Hallett-Mossop rime splintering dims the Southern Ocean: New insight from global cloud-resolving simulations

Rachel Atlas[1,1,1], Christopher S. Bretherton[1,1,1], Marat Khairoutdinov[2,2,2], and Peter N. Blossey[1,1,1]

[1]University of Washington
[2]SUNY

November 30, 2022

Abstract

In clouds containing both liquid and ice that have temperatures between -3°C and -8°C, liquid droplets collide with large ice crystals, freeze, and shatter, producing a plethora of small ice splinters. This process, known as Hallett-Mossop rime splintering, can cause clouds to reflect less sunlight and to have shorter lifetimes. Here, we use a novel suite of five global cloud-resolving models, which break up the Earth's atmosphere into columns with 2-4 km horizontal edges, to show that this microscale process has global implications. Simulations that include Hallett-Mossop rime splintering have reduced cumulus cloud cover over the Southern Ocean and reflect 12 Wm^{-2} less sunlight back to space over the same region, better matching satellite observed radiative fluxes. We evaluate simulated clouds using high-resolution visible images from the Himawari satellite, and radar reflectivities and two-dimensional images of cloud particles from the SOCRATES aircraft campaign. Cumulus clouds from simulations with Hallett-Mossop rime splintering included have more realistic cloud morphology, cloud vertical structure and ice crystal properties. We show that Hallett-Mossop rime splintering is an important control on cumulus cloud cover and cloud radiative effects over the Southern Ocean, and that including it in simulations improves model performance. We also demonstrate the key role that global cloud-resolving models can play in detangling the effects of clouds on Earth's climate across scales, making it possible to translate the behavior of tiny cloud particles (10^{-8} m^2) to their impact on the radiative budget of the massive Southern Ocean basin (10^{14} m^2).

Hallett-Mossop rime splintering dims the Southern Ocean: New insight from global cloud-resolving simulations

R.L. Atlas[1], **C.S. Bretherton**[1,2], **M.F. Khairoutdinov**[3], **P.N. Blossey**[1]

[1]Dept. of Atmospheric Sciences, University of Washington, Seattle, WA
[2]Vulcan Climate Modeling, Seattle, WA
[3]School of Marine and Atmospheric Sciences, Stony Brook University, Stony Brook, NY

Key Points:

- Including secondary ice production in simulations reduces summertime Southern Ocean cloud shortwave forcing by 12 Wm^{-2}
- Cumulus cloud fraction is highly sensitive to the inclusion of secondary ice production
- Global cloud-resolving simulations are invaluable for investigating climate impacts of small-scale cloud processes

Corresponding author: Rachel Atlas, `ratlas@uw.edu`

Abstract

In clouds containing both liquid and ice that have temperatures between -3°C and -8°C, liquid droplets collide with large ice crystals, freeze, and shatter, producing a plethora of small ice splinters. This process, known as Hallett-Mossop rime splintering, can cause clouds to reflect less sunlight and to have shorter lifetimes. Here, we use a novel suite of five global cloud-resolving models, which break up the Earths atmosphere into columns with 2-4 km horizontal edges, to show that this microscale process has global implications. Simulations that include Hallett-Mossop rime splintering have reduced cumulus cloud cover over the Southern Ocean and reflect 12 Wm^{-2} less sunlight back to space over the same region, better matching satellite observed radiative fluxes. We evaluate simulated clouds using high-resolution visible images from the Himawari satellite, and radar reflectivities and two-dimensional images of cloud particles from the SOCRATES aircraft campaign. Cumulus clouds from simulations with Hallett-Mossop rime splintering have more realistic cloud morphology, cloud vertical structure and ice crystal properties. We show that Hallett-Mossop rime splintering is an important control on cumulus cloud cover and CREs over the Southern Ocean, and that including it in simulations improves model performance. We also demonstrate the key role that global cloud-resolving models can play in detangling the effects of clouds on Earths climate across scales, making it possible to translate the behavior of tiny cloud particles (10^{-8} m^2) to their impact on the radiative budget of the massive Southern Ocean basin (10^{14} m^2).

Plain Language Summary

When clouds contain both liquid water and ice, liquid and frozen cloud particles compete with each other for water molecules. Frozen particles are larger than liquid particles so they fall faster under the influence of gravity. If frozen particles win the competition, they will efficiently remove water molecules from the cloud as they fall to the surface as snow. With too few water molecules, the cloud cannot persist and it dissipates. Here, we examine a set of five simulations that represent the entire atmosphere as a set of 42 million columns, each with 74 vertical levels. The five simulations use different combinations of formulas to control the rate at which frozen particles are produced within clouds. We find that the simulations which allow liquid particles to produce small frozen particles as they freeze and shatter, a process known as Hallett-Mossop rime splintering, can swing the competition towards ice within cumulus clouds over the Southern Ocean.

The causes the edges of the cumulus clouds to dissipate, which makes them narrower. We find that these narrower clouds look more like the clouds that exist in the real atmosphere and so we conclude that Hallett-Mossop rime splintering should be included in simulations.

1 Introduction

In mixed-phase clouds, liquid and frozen particles compete with each other for water vapor (Bergeron, 1928). Glaciation occurs when frozen particles out-compete liquid particles and the cloud condensed mass goes from predominantly liquid to predominantly frozen. Glaciation can alter cloud optical properties (Sun & Shine, 1994), increase precipitation, and reduce cloud lifetime (Rogers & Yau, 1996).

Ice crystals in clouds form via three different pathways: on ice nucleating particles (INPs), through the spontaneous freezing of water droplets at temperatures below -38°C, and via ice-liquid or ice-ice interactions (Pruppacher et al., 2010). The first two pathways are known as heterogeneous nucleation and homogeneous nucleation, respectively, and, together, they make up primary ice production. The third process is known as secondary ice production or ice multiplication. Above -38°C, the number of ice crystals that can be formed via primary ice production is capped by the number of INPs present in the atmosphere. Brewer and Palmer (1949) speculated that secondary ice production "may permit a water cloud to change to an ice cloud even though the number of ice-forming nuclei initially present is inadequate." In the seven decades that followed, numerous field campaigns have observed ice crystal concentrations which are orders of magnitude higher than INP concentrations (Field et al., 2016), attesting to the ubiquity of secondary ice production in mixed-phase clouds, and confirming that speculation.

Evidence of secondary ice production has been observed at all latitudes (Koenig, 1963; Hobbs & Rangno, 1985; Rangno & Hobbs, 2001; Heymsfield & Willis, 2014; Taylor et al., 2016; Huang et al., 2017; Ladino et al., 2017) but here we focus on low clouds over the vast Southern Ocean, which control the albedo of the Southern Hemisphere (Vonder Haar & Suomi, 1971) and are thus critically important for global climate. These clouds may become brighter or more long-lived as the climate warms, if increased atmospheric temperatures cause them to produce less ice and retain more supercooled water (Mitchell et al., 1989). Constraining the magnitude of this negative climate feedback has remained elusive due to an incomplete understanding of how ice particles form within Southern Ocean mixed-phase clouds. Recently, several studies have pointed to a strong influence of secondary ice production in these clouds. Indicators of secondary ice production within Southern Ocean cumuli have been identified in two different in-situ datasets (Huang et al., 2017; Scott, 2019), while two modelling studies have identified secondary ice production as an important and underappreciated control on the Antarctic radiative budget via the modulation of coastal stratus cloud properties (Young et al., 2019; Sotiropoulou et al., 2021). However, to our knowledge, no study has quantified the global radiative impact of secondary ice production in Southern Ocean clouds, which is a necessary step in constraining global cloud-climate feedbacks. Here, we use hindcasts made with a suite of global cloud-resolving models to show that secondary ice production is a strong control on Southern Ocean cloud albedo and is the largest source of inter-model variability in Southern Ocean cloud radiative effects and model performance across our set of simulations. We use in-situ aircraft observations and satellite data to show that more realistic cloud morphologies, cloud microphysics and cloud radiative effects are found in simulations that include secondary ice production.

2 Datasets

2.1 Global Cloud-Resolving Simulations

Our simulations are run using the global version of the System for Atmospheric Modelling, or GSAM (Stevens et al., 2019). GSAM is anelastic and includes a comprehensive land-surface model and a mixed-layer ocean. The simulations analyzed here are run with CAM3 radiation (Collins et al., 2006) and a grid spacing of 4 km at the equator and 2-3 km over the Southern Ocean. They have 4608 x 9216 horizontal grid cells and 74 vertical levels. Five-day simulations are run with five different microphysics schemes but otherwise identical model setups. To allow the model time to spin up, we have excluded the first day of the simulation in all of the analyses shown in this study. Simulated temperature and horizontal winds are initialized with and nudged to ERA5 reanalysis with a timescale of 24 hours, tightly constraining the synoptic dynamics, as in Gettelman et al. (2020) and Zhou et al. (2021). This has two key advantages. The first is that the model output can faithfully be compared with coincident real-world observations. The second is that it makes certain that differences in the model output between different simulations necessarily arise from differences in the model microphysics.

We show animations of albedo from two GSAM simulations in Appendix A to give a general sense of how clouds are represented in the simulations. GSAM simulations are run from 0 UTC on February 16th to 0 UTC on February 21st 2018, which overlaps three research flights from the Southern Ocean Clouds, Radiation, Aerosol Transport Experimental Study (SOCRATES) (McFarquhar et al., 2020). Throughout this study, we evaluate GSAM using observations from two of these research flights, as described in Section 2.2. In Appendix B, we show that concentrations of frozen particles imaged by the Two-Dimensional Stereo Probe (2D-S) (Atlas et al., 2021) during SOCRATES are much larger than typical INP concentrations from sea spray aerosol to show that secondary ice production is active in SOCRATES-sampled clouds.

GSAM simulations are run with a suite of microphysics schemes that span the range of complexity exhibited by bulk schemes. A useful proxy for the complexity and costliness of bulk microphysics schemes is the number of prognostic variables that they use. Table 1 lists the five different microphysics schemes used, the number of prognostic variables they use, and the modes of primary and secondary ice production that are active within each scheme, in their implementations in GSAM. Note that the one-moment SAM microphysics scheme, SAM1MOM, (Khairoutdinov & Randall, 2003) does not include primary or secondary ice production because condensed cloud and precipitation mass is partitioned into liquid and ice based on temperature. Therefore, it will not be mentioned below when the primary and secondary ice formation mechanisms in the other schemes are described. All simulations are run with a fixed cloud liquid droplet number concentration of 100 cm^{-3}.

The clouds analyzed in this study occur at temperatures above -38°C so heterogeneous ice nucleation accounts for all primary ice production. As shown in Table 1, heterogeneous ice nucleation is represented differently in the five different microphysics schemes used here. Thompson (Thompson et al., 2008), P3 (Morrison & Milbrandt, 2015), and M2005 (Morrison et al., 2005) allow deposition nucleation (also referred to as deposition/condensation nucleation), and immersion freezing for both cloud drops and raindrops. Immersion freezing is parameterized following Bigg (1953) and produces far fewer particles than deposition freezing in the clouds examined here. In all three implementations, the concentration of INPs for deposition freezing is prescribed as a function of temperature following the Cooper curve (Cooper, 1986, Figure B1). In M2005 and Thompson, deposition nucleation occurs in two situations: 1) when ice supersaturation exceeds a fixed thresh-

Table 1. Characteristics of the five microphysics schemes used here

Microphysics Scheme	Prognostic Variables	Heterogeneous Nucleation	Secondary ice production
SAM1MOM	2	None	None
Thompson	7	Deposition	Hallett-Mossop rime splintering
P3	8	Deposition, Immersion, Raindrop Freezing	None
M2005	10	Contact, Deposition, Immersion, Raindrop Freezing	Hallett-Mossop rime splintering in high clouds
M2005 MOD	10	Contact, Deposition, Immersion, Raindrop Freezing	Hallett-Mossop rime splintering

old (8% in M2005, 25% in Thompson) or 2) in air that is saturated with respect to liquid and colder than -12°C. In P3, it occurs when the temperature is below -15°C and ice supersaturation is above 5%. M2005 also includes contact freezing at temperatures below -4°C, for which the concentration of INPs is prescribed as a function of temperature following the Meyers curve (Meyers et al., 1992, Figure B1). The Meyers curve prescribes higher concentrations of INPs than the Cooper curve for the same temperatures, and contact freezing operates in a wider range of atmospheric conditions. For these reasons, contact freezing dominates the primary ice production in M2005, and M2005 has much stronger primary ice production than either Thompson or P3.

The Thompson and M2005 schemes include parameterizations of Hallett-Mossop rime splintering (HMRS), a type of secondary ice production that occurs at temperatures between -3°C and -8°C (Hallett & Mossop, 1974). HMRS involves large frozen particles, small droplets and large droplets and can be conceptualized as a two-step process (Field et al., 2016). In the first step, small droplets freeze onto large frozen particles and largely retain their shapes to create an icy shell with narrow protrusions. In the second step, large droplets freeze and shatter when they come into contact with those small protrusions. HMRS is parameterized in M2005 and Thompson as a single-step process; at each microphysics time step, the bulk mass of supercooled water rimed onto large frozen particles is computed as a function of droplet mass, and the size and number of the large frozen particles. The number of ice splinters produced is then parameterized as a function of the rimed mass and the temperature. The number of splinters produced per unit of rimed mass maximizes at -5°C and decays towards -3°C and -8°C.

While M2005 and Thompson permit HMRS over the same range of temperatures, M2005 has additional, stricter requirements for when HMRS can occur. As described in Atlas et al. (2020), M2005 requires either that the droplet mass is greater than 0.5 g kg^{-1} or that the rain mass is greater than 0.1 g kg^{-1}, and that either graupel, snow or ice mass exceeds 0.1 g kg^{-1}. While virtually all mixed-phase clouds within the Hallett-Mossop temperature range will satisfy the conditions for HMRS in the Thompson scheme, low clouds rarely satisfy the stricter conditions for HMRS in M2005. Thus, the fifth simulation that we run is a modified version of M2005, which we refer to as 'M2005 MOD', with all mass thresholds removed from the HMRS parameterization so that the process can occur in low clouds. Throughout this study, we refer to M2005 as a simulation without HMRS because we focus primarily on low clouds but that characterization is not accurate for all cloud regimes.

2.2 Satellite and Aircraft Observations

We use CERES level 3 data (Doelling et al., 2013; NASA/LARC/SD/ASDC, 2017), obtained from the NASA Langley Research Center Atmospheric Science Data Center, to constrain global CREs. This dataset has 1° x 1° horizontal resolution and hourly temporal resolution. We use high-resolution observations from Himawari (Smith & Minnis, 2020) to qualitatively compare cloud morphology between GSAM and the real world. Retrievals of broadband shortwave albedo from Himawari from the spatial and temporal ranges of interest were performed by NASA Langleys Satellite Cloud and Radiation Property retrieval System (SatCORPS). This data has 0.5 to 2 km horizontal resolution and either 10-minute or 30-minute time resolution depending on the time of day.

We use in-situ airborne observations and remote sensing data collected by the NSF/NCAR Gulfstream-V HIAPER (High-Performance Instrumented Airborne Platform for Environmental Research) during SOCRATES to evaluate representations of the boundary layer and low clouds in GSAM. GSAM simulations overlap three research flights from SOCRATES: 1) RF11 on February 17th, 2018, which sampled open-cell cumulus between -9°C and 0°C, 2) RF12 on February 17th-18th, 2018, which sampled stratocumulus between -7° and -3°, and 3) RF13, on on February 19th-20th, 2018, which sampled stratocumulus between -3°C and 2°C. Since RF13 did not sample clouds within the Hallett-Mossop temperature range, we only compare GSAM output with observations from RF11 and RF12. Simulated boundary layer thermodynamics are evaluated with in-situ temperature and water vapor measurements (EOL, 2019), and simulated cloud microphysics are evaluated with single-particle phase classifications of particles with projected areas $\geq 2500\ \mu m^2$ that were imaged by the Two-Dimensional Stereo Probe (2D-S) (Atlas et al., 2021), particle concentrations from the Cloud Droplet Probe (CDP) (EOL, 2019), and radar reflectivities from the W-band HIAPER cloud radar (EOL, 2018).

3 Results

3.1 Comparisons with satellite

Figure 1 compares simulated global cloud radiative effects (CREs) at top of atmosphere from all five GSAM simulations with retrieved CREs from CERES. We coarsen the GSAM output to 1° x 1° in order to compare with CERES. Here and throughout the study, red lines indicate simulations with HMRS and blue lines indicate those without. The orange box highlights the Southern Ocean region. In the tropics, longwave radiation dominates the variance and the bias in simulated CREs. In the Southern Ocean, shortwave radiation dominates the biases. All simulations have too much reflected shortwave radiation over the Southern Ocean, opposite to the bias historically exhibited by most climate models (Trenberth & Fasullo, 2010). GSAM simulations with HMRS have an average SW CRE of 7.5 W m^{-2} over the Southern Ocean (42°S - 60°S), compared to 19.4 W m^{-2} for simulations without HMRS. Thus, simulations with HMRS have a reduced SW bias by about 12 Wm^{-2}. The blue and red solid lines represent M2005 and M2005 MOD, respectively, and we can be certain that the differences between those two simulations are solely due to the activation of HMRS in low clouds.

We compare visible albedo between the Himawari satellite and GSAM to investigate if cloud cover and cloud brightness can explain the trends seen in the radiative biases (Figure 2). Throughout this study, figures with grey borders show comparisons that

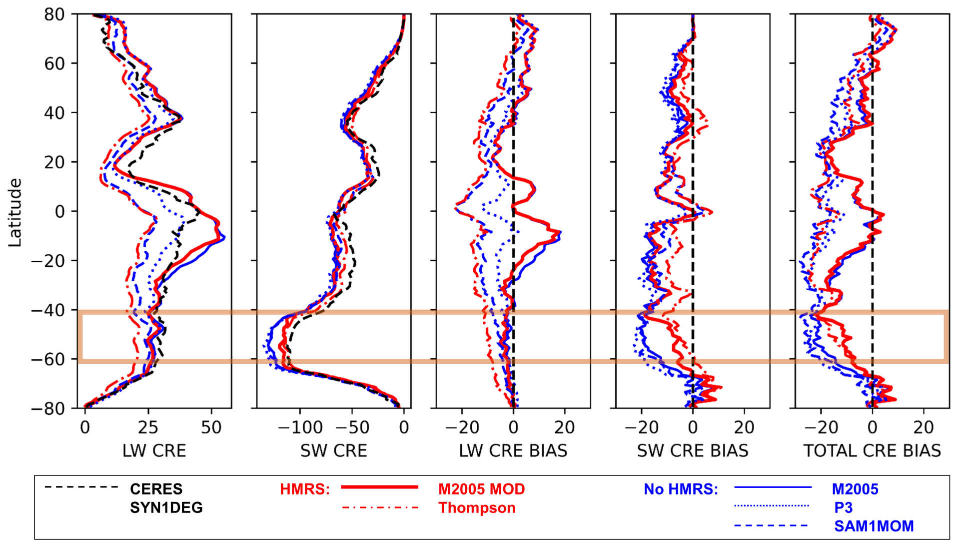

Figure 1. Zonal average longwave and shortwave cloud radiative effects (CREs) at top of atmosphere are shown for the five GSAM simulations and for CERES SYN1DEG in the first and second columns, respectively, averaged over the four-day period from 0 UTC on February 17th to 0 UTC on February 21st, 2018. Biases in longwave, shortwave, and total simulated CREs compared to CERES (GSAM-SYN1DEG) are shown in the third, fourth and fifth columns, respectively. The orange box highlights the latitudinal range of interest (42° - 60°S). Simulations with Hallett-Mossop rime splintering included ("HMRS") are in red, and simulations without it ("No HMRS") are in blue.

are limited to the SOCRATES study region, because they evaluate GSAM using Himawari and/or in-situ observations. In Figure 2, our analysis is restricted to the region for which high resolution Himawari data is available (40°-68°S, 130°-165°E). The snapshots shown in Figures 2a and 2b are coincident with SOCRATES flights RF11 and RF12, respectively, and the SOCRATES flight tracks are overlaid on the albedo maps in red. RF11 sampled open cell cumulus while RF12 sampled the stratocumulus cloud deck south of the open cell region. Simulations with HMRS are in the top row and simulations without it are in the bottom row.

Low stratus clouds and high/frontal clouds are too bright in all simulations in both snapshots. This may account for the overall bright bias seen in all simulations. Simulations without HMRS are also too bright in the open cell regions, due to the larger cloudy area surrounding each cumulus cloud center. In other words, all simulations have a similar number of cumulus clouds, but simulations without HMRS have more horizontal cloud cover associated with each cumulus cloud. Simulations with HMRS are dimmer in the open cell regions due to smaller cumulus cloud cover and bear a closer resemblance to the snapshots from the Himawari satellite.

This qualitative comparison suggests the cumulus regime accounts for the smaller shortwave CREs and better model performance exhibited by simulations with HMRS (Figure 2). However, if there is variance in the brightness of the stratiform clouds between the different simulations, it may be difficult to detect by eye from the albedo maps. In order to verify that cumulus clouds are responsible for the discrepancy in shortwave CREs across the models, we create a “cloud mask” to classify model output into four different cloud regimes: low cloud fraction (including clear sky), high clouds, low stratus clouds, and low cumulus clouds. We use the output of the M2005 MOD simulation to create the cloud mask, as discussed in Appendix C. Because all five GSAM simulations are nudged to the same reanalysis, they typically simulate the same cloud morphologies in the same locations, and the mask based on M2005 MOD can be faithfully applied to all simulations. In the following, locations where the simulated cloud morphology disagrees with observations will be noted. However, as our focus is on the impact of changes in simulated cloud due to differing microphysical parameterizations, it is valuable to use a mask that behaves consistently across the simulations.

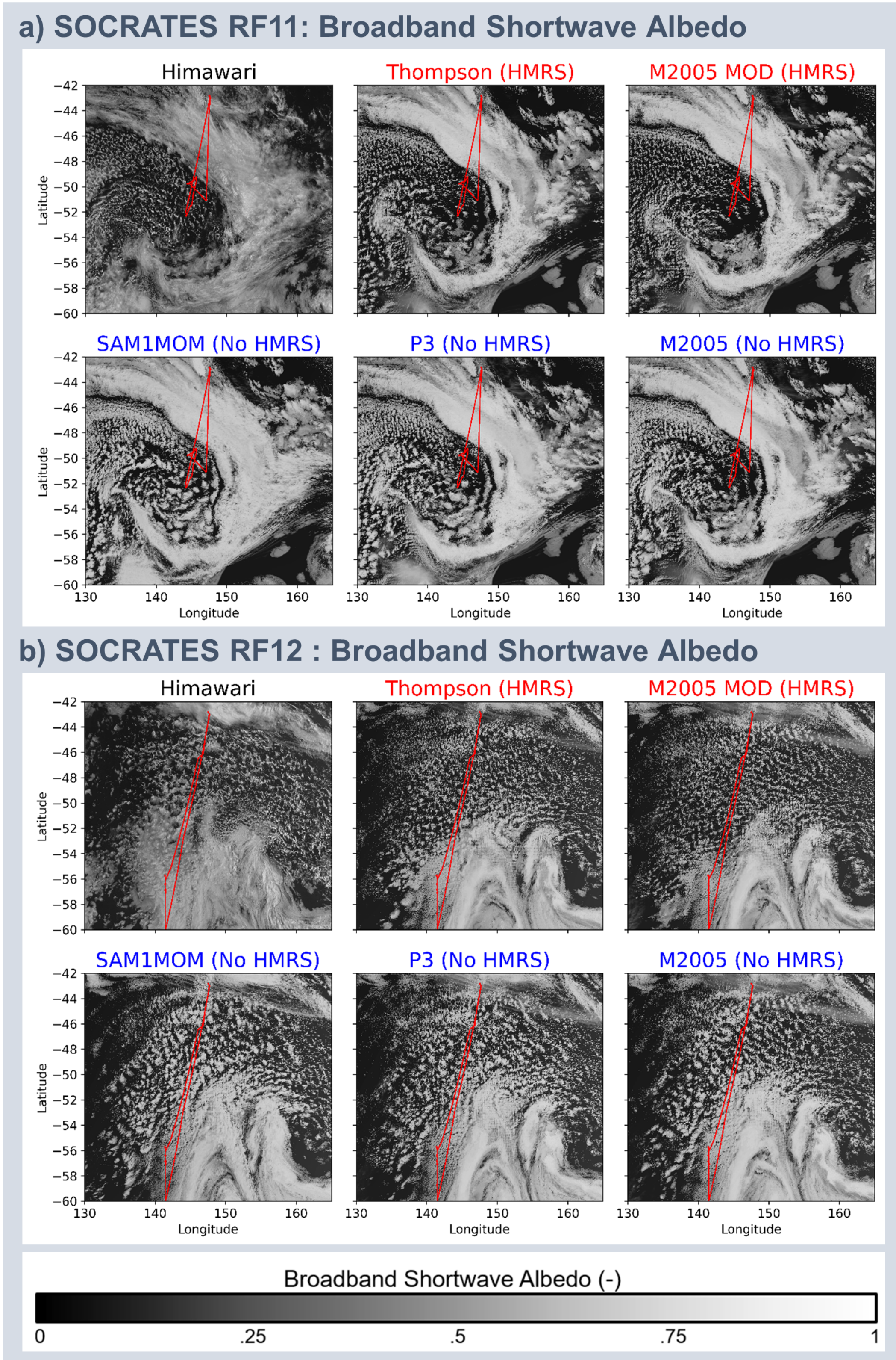

Figure 2. Coincident snapshots of visible cloud albedo are shown for the Himawari satellite and the five GSAM simulations for the SOCRATES sampling region. The snapshot in (a) at 3 UTC on February 17th 2018 coincides with SOCRATES RF11 which sampled open cell cumulus and the snapshot in (b) at 6 UTC on February 18th 2018 coincides with SOCRATES RF12 which sampled stratocumulus. Red lines indicate SOCRATES flight tracks. Simulations with

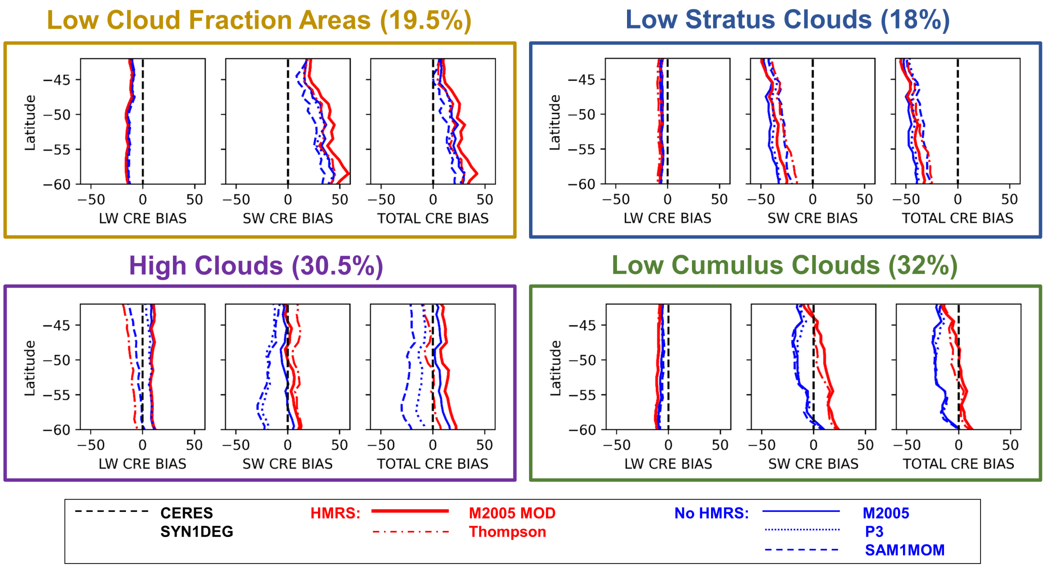

Figure 3. Zonal average biases in longwave, shortwave, and total simulated CREs compared to CERES (GSAM-SYN1DEG) are shown for the latitudinal range of interest (40°-60°S), for the four cloud regimes averaged over the four-day period from 0 UTC on February 17th to 0 UTC on February 21st, 2018. Simulations with Hallett-Mossop rime splintering included ("HMRS") are in red, and simulations without it ("No HMRS") are in blue.

We compare CREs between CERES and GSAM separately for the four different cloud regimes in Figure 3. Low cloud fraction areas are too dim in all simulations because these regions contains clouds that have broken up prematurely in the GSAM simulations. For example, in the lower right corner of the albedo maps in Figure 2a, the five GSAM models simulate mainly clear sky but Himawari shows a robust stratiform cloud deck.

Low stratus regions are too bright in all simulations and the magnitude of the bias is similar for simulations with and without HMRS. Differences in high clouds account for most of the variance in longwave CREs. There is also a large spread in the shortwave CREs for high clouds, with SAM1MOM and P3 exhibiting substantial bright biases. However, these bright biases cannot be explained by the exclusion of HMRS because M2005 does not exhibit the same bias. We will evaluate the representation of high clouds in GSAM more thoroughly in a future study.

Low cumulus clouds are the only cloud regime for which the shortwave CREs exhibit an unambiguous dependence on the inclusion of HMRS. Low cumulus clouds from simulations with HMRS have smaller biases in the total CRE, due in part to compensating biases in the shortwave and longwave CREs. The examples in Figure 2 show that simulations with HMRS simulate cumulus cloud morphologies that agree well with Himawari, but cumulus cloud regimes from those simulations reflect less shortwave radiative then what was observed. This is because there are regions where stratocumulus decks have broken up into open cell cumulus prematurely in the simulations and, in those regions, we are comparing dimmer simulated cumulus clouds with brighter observed stratocumulus clouds. An example of such a region can be seen in Figure 2b, around 140°E and between 52°S and 54°S. In that region, all five simulations produce open cell cumulus but Himawari shows that a stratocumulus was present in reality. Because the cloud mask is based on the output of M2005 MOD, this area is classified as low cumulus.

Thus far, we have shown that simulations with HMRS simulate dimmer Southern Ocean clouds and agree better with satellite observations from Himawari and CERES. Furthermore, the inclusion of HMRS in simulations primarily affects shortwave CREs by reducing the cumulus cloud fraction. At this point, it is reasonable to ask whether these improvements are related to increased physical realism of the simulated clouds or caused by offsetting errors. In other words, have simulated cumulus clouds improved for the right reasons? In the following section, we address this question by using in-situ observations to determine if simulations with HMRS have more realistic cloud microphysics.

3.2 Comparisons with aircraft data

Throughout this section, we compare GSAM output with in situ and remote sensing data from two SOCRATES flights, RF11 and RF12. To evaluate simulated microphysics, liquid and frozen simulated particle size distributions (PSDs) are evaluated with SOCRATES-observed PSDs from the CDP and 2D-S instruments (Figure 4). The two SOCRATES flights shown in Figure 2, RF11 and RF12, both sampled clouds within the HMRS temperature range. RF12 sampled a stratocumulus cloud deck that fully overlapped the HMRS temperature range, collecting 1142 seconds of particle observations at all heights within the cloud. RF11 collected 176 seconds of particle observations, mainly at a single height within a cumulus cloud field. Thus, we use RF12 for this analysis. The simulations are sampled along the flight track, meaning that nearest neighbors in space and time are extracted from the model output for every 10 seconds of in-situ sampling, and averaged together. Although CREs of stratiform cloud regions are not sensitive to the inclusion of HMRS in these simulations (Figure 3), we hypothesize that the inclusion of HMRS affects cloud microphysical properties of stratiform clouds in largely the same way that it affects cumulus clouds. Atlas et al. (2020) developed an LES case study based on RF12 and found that simulated PSDs from M2005 MOD had more large frozen particles and agreed better with SOCRATES observations than M2005. That result is replicated here, as M2005 MOD has concentrations of large frozen particles that are three orders of magnitude higher than in M2005 and has the best agreement with SOCRATES PSDs out of the five microphysics schemes (Figure 4).

Thompson has more large frozen particles than any of the simulations except M2005 MOD and partially replicates the observed large frozen particle mode. The three simulations without HMRS do not have enough large frozen particles. We note that SAM1MOM does not assume size distributions for cloud droplets and cloud ice so those two hydrometeor classes are excluded from the SAM1MOM PSDs. However, since most of the large frozen particles are contained in the snow and graupel classes, we do not expect the absence of cloud ice to affect our conclusions. Thus, the inclusion of HMRS in the simulations improves simulated cloud microphysics in stratiform clouds within the HMRS temperature range. Although in situ sampling of PSDs during RF11 was not statistically representative, remote sensing from the HIAPER cloud radar gathered a larger sample of data that can be used to evaluate the simulated cloud and precipitation features in the cumulus regime.

We compute synthetic radar reflectivities for the five GSAM simulations using a modified version of QUICKBEAM (Haynes et al., 2007). QUICKBEAM is Fortran-based software that uses microphysics information to estimate radar reflectivities. It has been implemented to run online with M2005 and Thompson microphysics within the SAM LES (Atlas et al., 2020). Here, we develop a modified version of QUICKBEAM written in Python which runs offline and is compatible with all five microphysics schemes used here. The PSDs specified within the microphysics schemes and shown in Figure 4 are used to compute radar reflectivities. Thus, radar reflectivities computed for SAM1MOM do not include contributions from cloud droplets and cloud ice. The original QUICKBEAM software accounts for attenuation due to gases and hydrometeors along the radar path for a space-based or ground-based radar, but is not included here because the changing po-

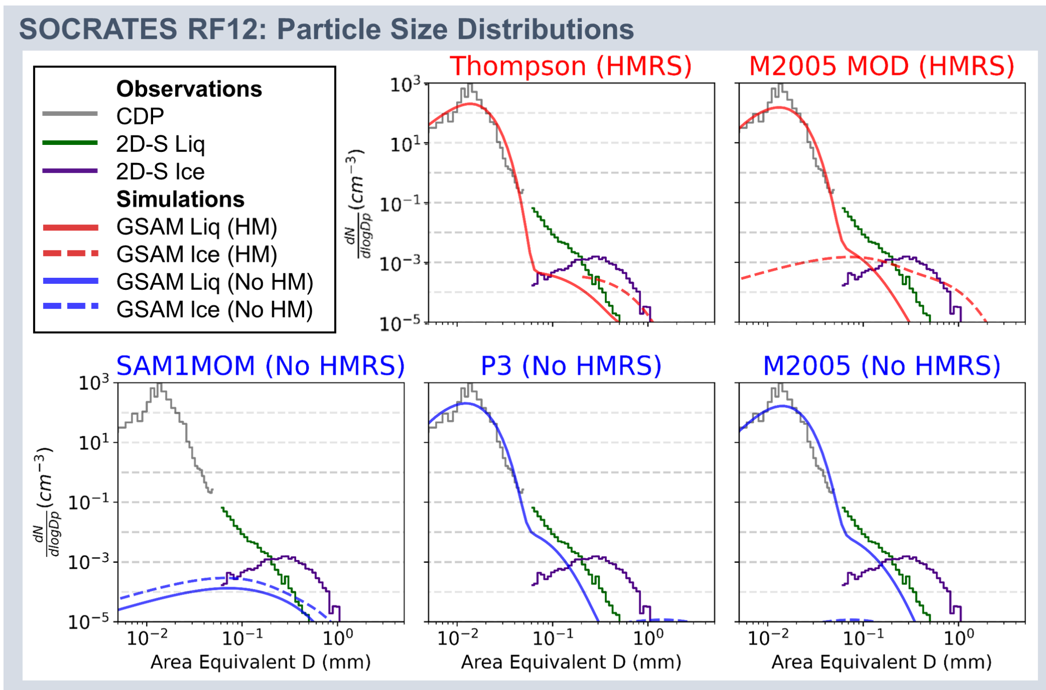

Figure 4. Liquid (solid lines) and frozen (dashed lines) simulated PSDs are compared with observed PSDs from SOCRATES. Grey lines are observed droplet concentrations from the CDP, green lines are observed large droplet concentrations from the 2D-S, and purple lines are observed frozen particle concentrations from the 2D-S. Simulations with Hallett-Mossop rime splintering incuded ("HMRS") are in red in the top row, and simulations without it ("No HMRS") are in blue in the bottom row. Simulations have been sampled along the flight track.

sition of the aircraft complicates the calculation of attenuation and because attenuation is usually small for low clouds and for an airborne radar which profiles clouds at a close range. However, we caution that high radar reflectivities (> 5 dBZ) may be overestimated due to unaccounted for hydrometeor attenuation.

Figure 5 compares radar reflectivities and cumulus cloud texture between GSAM output and observations from Himawari and the HIAPER radar. The observed cumulus and the simulated cumulus from the simulations with HMRS are dominated by narrow banded structures (second column of Figure 5), resembling the "gravel" pattern from Stevens et al. (2020). Simulated cumulus from the simulations without HMRS feature wider and puffier cumulus clouds (fourth column of Figure 5), resembling the "flowers" pattern from Bony et al. (2020). The synthetic reflectivities from all simulations are dominated by columns, which span the height from the sea surface to the cloud tops, indicating the presence of precipitation; these are associated with cumulus cloud centers. The simulations without HMRS have more nonprecipitating "interstitial" cloud with low reflectivities, indicating the absence of large particles, between the columns. The interstitial cloud contributes to the footprint of the simulated cumulus clouds in the albedo maps.

To test whether the HMRS or no-HMRS simulations better match the radar observations, we compute a vertical profile of "reflectivity fraction", which is the fraction of radar reflectivities that are greater than -50 dBZ, as a function of height. The reflectivity fraction is sensitive to both cloud and precipitation but it can be used a proxy for cloud fraction in the upper part of the boundary layer. We use model output from the area shown in the albedo maps in Figure 5 (49-52.5°S, 144-146.5°E), and from 3, 4 and 5 UTC on February 17th 2018, to compute the reflectivity fraction for the simulations. The observed reflectivity fraction is based on the reflectivities shown in the upper left panel in Figure 5.

Figure 6a shows observed and simulated profiles of temperature, specific humidity and reflectivity fraction. Profiles of temperature and humidity verify that the simulations are accurately representing the thermodynamics of the boundary layer. The observations and the two simulations with HMRS have peaks in reflectivity fraction at about 1 km, which is below the Hallett-Mossop temperature range. The three simulations without HMRS have higher reflectivity fractions throughout the Hallett-Mossop temperature range. Furthermore, they have peaks in reflectivity fraction that are either partially or

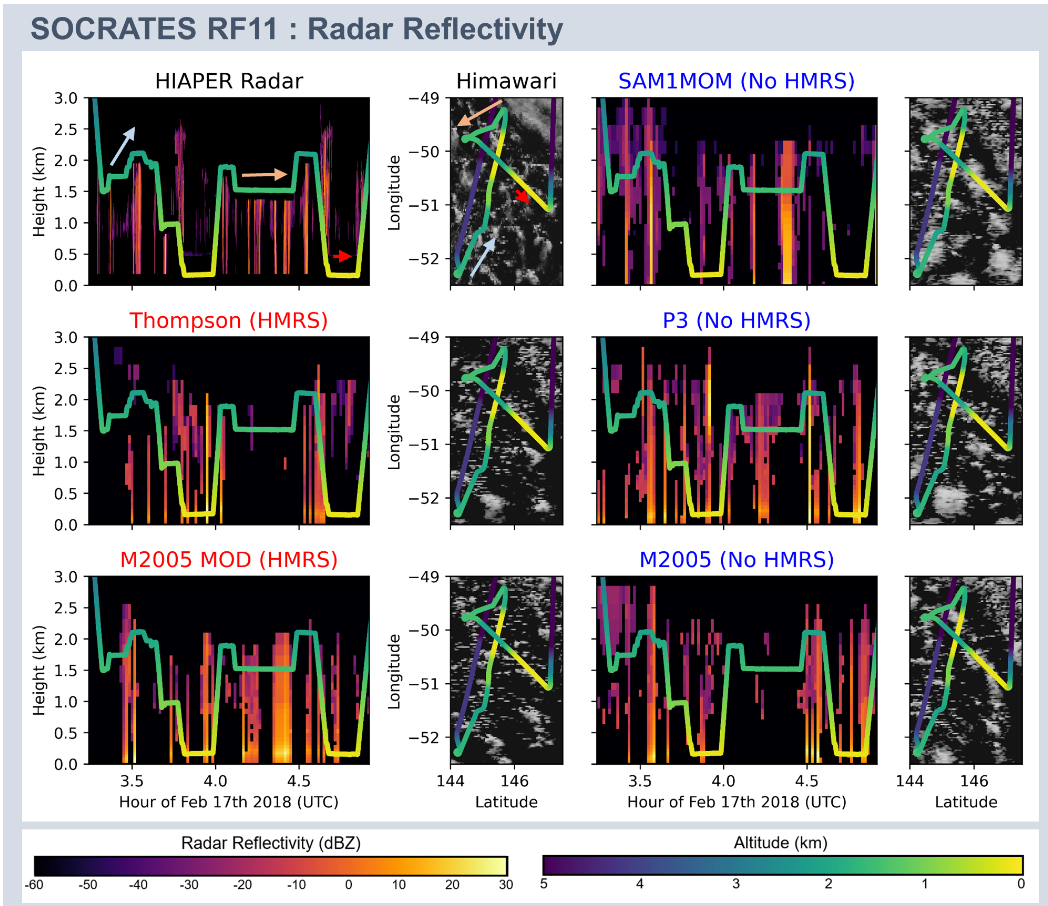

Figure 5. Radar reflectivity and visible albedo maps are shown for the observations (top left) and the five GSAM simulations. Flight tracks, color-coded by aircraft altitude, are shown on all plots. The arrows on the two plots in the upper left corner show how to align the two perspectives. Simulations with Hallett-Mossop rime splintering included ("HM") are in the left column (below the observations), and simulations without it ("No HMRS") are in the right column.

fully within the Hallett-Mossop temperature range. Their higher reflectivity fractions are due to the presence of interstitial clouds. The lower observed reflectivity fraction indicates that little interstitial cloud was present in the real atmosphere, in agreement with the simulations with HMRS.

We showed in Section 3.1 that simulations with HMRS have more realistic shortwave CREs over the Southern Ocean because they have less cumulus cloud cover. In this section, we showed that these simulations also have more realistic cloud microphysics. They simulate a larger number of frozen particles, in agreement with in-situ observations, and less interstitial cloud, in agreement with the HIAPER radar. These comparisons also illuminated how HMRS reduces cumulus cloud fraction and are summarized in Figure 6b.

In all simulations, updrafts occur preferentially in moist columns within the boundary layer and form cumulus cloud centers. Interstitial cloud can detrain into the drier air between the cumulus cloud centers. The synthetic reflectivities show that the interstitial clouds are thin and lack large particles, making them more susceptible to glaciation than the cumulus cloud centers. In the simulations with HMRS, ice formation is efficient and ice crystals out-compete liquid particles within the detrained interstitial cloud, glaciating it and drastically reducing its lifetime. In the simulations without HMRS, ice formation is suppressed and the interstitial clouds persist, reflecting excessive sunlight back to space over the Southern Ocean.

4 Conclusions

We have analyzed supercooled boundary layer clouds over the Southern Ocean in a unique suite of five meteorologically-nudged global cloud-resolving simulations of a 5-day period during Feb. 2018 during the SOCRATES field study. The simulations differ only in their cloud microphysics parameterizations, which include several widely-used schemes. We compared them with satellite, in-situ and radar observations. Our key finding is that, in simulations that include Hallett-Mossop rime splintering (a form of secondary ice production), shallow cumulus clouds glaciate over the Southern Ocean, decreasing the surrounding cover of detrained "interstitial" cloud and reducing the regionally-averaged shortwave cloud radiative effect biases by 12 $\mathrm{Wm^{-2}}$. Simulations including secondary ice production have more frozen particles in low clouds, consistent with in-situ

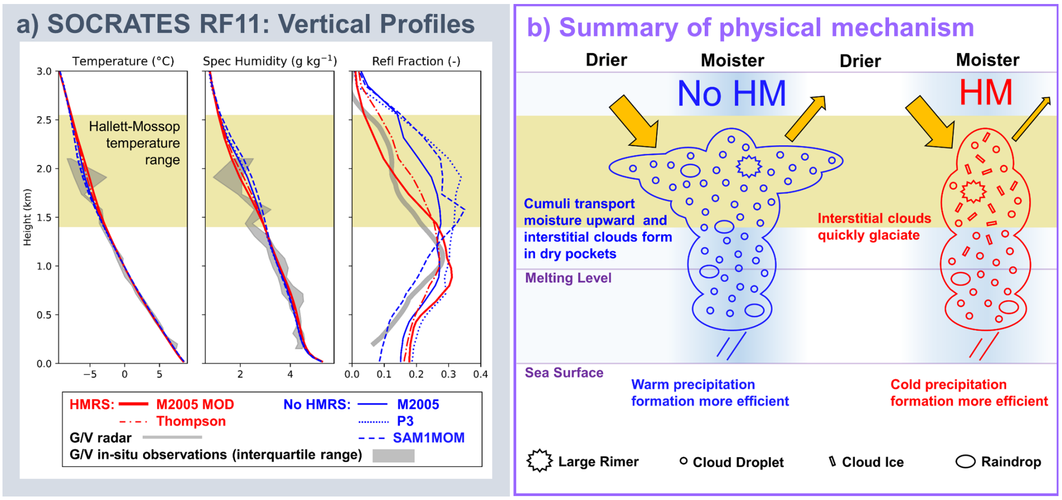

Figure 6. a) Profiles of temperature, specific humidity, and reflectivity fraction are shown, from left to right. Simulations with Hallett-Mossop rime splintering included ("HMRS") are in red and simulations without it ("No HMRS") are in blue. b) Schematic showing how HMRS reduces cumulus cloud fraction.

observations, and their reduced overall albedo over the Southern Ocean agrees better with satellite observations.

Our study illuminates the importance of secondary ice production to Earth's climate. It exemplifies how global cloud-resolving simulations, which can simulate supercooled cloud fields much more realistically than conventional coarse-grid climate models, are uniquely suited for evaluating and testing the global or regional climate impacts of small-scale microphysical processes. Large eddy simulations, which have very fine grids but only cover small computational domains, are also useful for investigating the detailed microphysics in boundary-layer clouds like those that have complex small-scale internal circulations. However, because they simulate only a small portion of the Earth, they cannot be used to comprehensively simulate interactions between clouds and meteorology to allow a reliable quantification of global or regional cloud radiative effects.

Other types of secondary ice production may be important in the real atmosphere. Recently, Luke et al. (2021) argued that freezing fragmentation (also referred to as droplet shattering), is stronger than rime splintering within the Hallett-Mossop temperature range in Arctic clouds. Sotiropoulou et al. (2020) combined Hallett-Mossop rime splintering with another secondary ice production process, mechanical breakup during ice-ice collisions, to explain observed ice crystal concentrations in Antarctic clouds. The glaciation mechanism we outline here is not specific to Hallett-Mossop rime splintering; any secondary ice process that produces frozen particles at a sufficient rate would glaciate the thinner parts of cumulus clouds. However, the detailed mechanism and temperature range are important to parameterizing secondary ice production and quantifying its radiative impacts.

Intriguingly, ice crystal concentrations were also observed to be greater than INP concentrations in SOCRATES-sampled clouds at temperatures down to -25°C, where Hallett-Mossop rime splintering is not active, indicating that other secondary ice processes are active at colder temperatures (Appendix B). We acknowledge that our simulations do not account for secondary ice production outside of the Hallett-Mossop temperature range, and we hope that future studies illuminate how secondary ice production influences Southern Ocean clouds at temperatures below -8°C.

We have not altered the formulation of primary ice production in the various microphysics schemes used in our simulations to account for low INP concentrations observed over the Southern Ocean. As discussed in Appendix B, primary ice production operates much more strongly in some schemes that in others, and the assumed INP concentrations are much larger than observed over the Southern Ocean. However, across our suite of simulations, the clouds are far less sensitive to differences in primary ice production between the microphysics schemes than they are to the inclusion of secondary ice production. This conclusion differs from Vergara-Temprado et al. (2018), who found that Southern Ocean clouds are highly sensitive to the representation of primary ice production.

In addition to the bright bias demonstrated by simulations without secondary ice production in Southern Ocean cumulus clouds, all simulations demonstrate a bright bias in Southern Ocean stratiform clouds. We hope that future studies can investigate its cause and propose effective solutions.

In light of its substantial effect on Earth's climate, we encourage climate modelers to account for secondary ice production in supercooled clouds such as those prevalent over the Southern Ocean and constrain those models with the increasing number of observational analyses becoming available. In particular, we recommend removing the mass thresholds from the parameterization of Hallett-Mossop rime splintering in the M2005

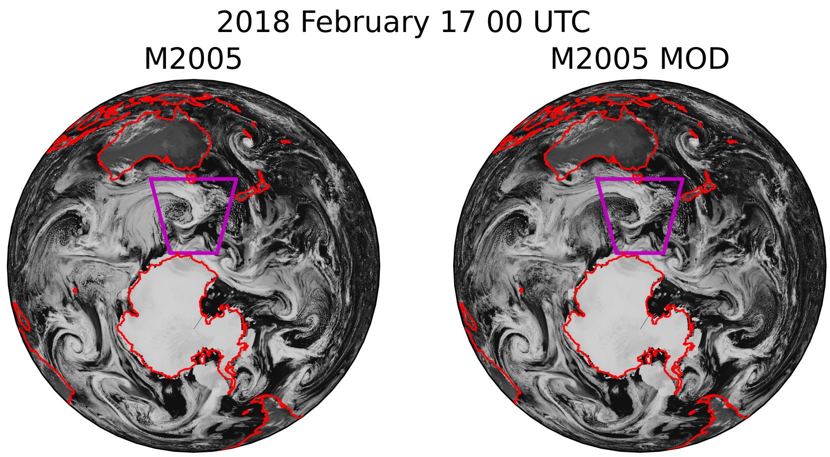

Figure A1. Animations of albedo from the M2005 and M2005 MOD simulations for the last four days of the simulation. The purple box highlights the SOCRATES study region.

microphysics scheme. We note that global (and boundary-forced regional) cloud-resolving models are an attractive testbed to capture the interplay of large scale meteorology and small scale cloud processes and we encourage their use in future investigations of cloud-climate interactions.

Appendix A Animations of albedo from GSAM

We show animations of visible albedo from two GSAM simulations, M2005 and M2005 MOD, in Figure A1. Animations show the last four days of the simulation (February 17th to February 20th). GSAM resolves clouds on a wide range of scales and simulates realistic cloud morphologies. M2005 has more cloud cover than M2005 MOD within the cumulus cloud regions.

Appendix B Evidence for Secondary Ice Production during SOCRATES

Figure B1 compares concentrations of ice crystals from SOCRATES with typical concentrations of INPs from sea spray aerosol for the range of temperatures sampled during SOCRATES. Marine aerosols are the predominant source of INPs over the Southern Ocean (McCluskey et al., 2019), so we expect that concentrations of INPs during the period of study are within the range of marine INP concentrations that have been reported in the literature. Ice crystal concentrations are estimated from 2D-S imaged particles that have been classified as frozen (Atlas et al., 2021), and INP concentrations are sourced from two studies. DeMott et al. (2016) includes INP concentrations from sea spray generated in wave channel experiments as well as from ambient marine boundary layer air sampled in the Carribean, the Pacific Ocean and the Arctic. McCluskey et al. (2018) quantified INPs within the Southern Ocean boundary layer using filter samples collected as part of The Clouds, Aerosols, Precipitation, Radiation, and atmospherIc Composition Over the southeRN ocean (CAPRICORN) campaign. We show data from DeMott et al. (2016) using a grey shaded region and we show data from McCluskey et al. (2018) using green stars, and we note that this representation is similar to Figure 2 in McCluskey et al. (2018). We show ice crystal concentrations from the two SOCRATES flights that we analyze throughout this study, which overlap the time period of the simulations.

Between -25°C and -20°C, median ice crystal concentrations are at the upper limit of reported marine INP concentrations and mean ice crystal concentrations are greater than reported marine INP concentrations. Between -20°C and -15°C, median and mean ice concentrations are one to two orders of magnitude higher than the upper limit of reported marine INP concentrations. These temperature ranges do not overlap the Hallett-Mossop temperature range, implying that other types of secondary ice production are occurring. There was not enough in-cloud data from these two flights in the range of -15°C to -10°C to include in this analysis, and there is little data on INP concentrations at temperatures above -10°C.

The large discrepancies between ice crystal concentrations and typical marine INP concentrations suggest that secondary ice production is the dominant mechanism of ice crystal formation in this subset of the SOCRATES dataset.

We also show two curves commonly used to prescribe INP concentrations for primary ice production in Figure B1. The Meyers curve (Meyers et al., 1992) is used for contact nucleation, which is active in the M2005 scheme. The Cooper curve (Cooper, 1986) is used for deposition nucleation, which is active in all microphysics schemes used here except SAM1MOM. Both curves drastically overestimate the concentration of INPs over the Southern Ocean. If secondary ice production is excluded, and primary ice production is implemented using one or both of these curves, then the number of ice crystals will be overestimated at the coldest temperatures examined here ($T <$ -20°C) and underestimated at temperature above -10°C.

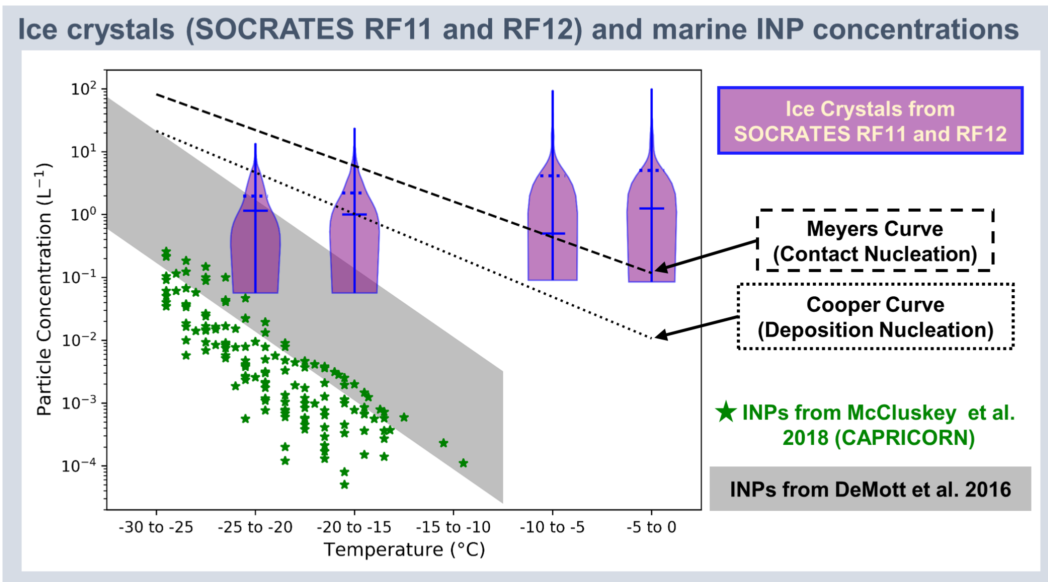

Figure B1. Purple and orange violin plots show distributions of ice crystal and INP concentrations, respectively, for 5° temperature brackets. Solid horizontal lines show median concentrations and dashed horizontal lines shown mean concentrations. Flights RF11 and RF12 from the SOCRATES dataset are used. The black lines show two different estimates of INP concentrations, modelled as exponential functions of temperature. Dashed and dotted lines show the Meyers curve, used for contact nucleation, and the Cooper curve, used for deposition/condensation nucleation, respectively.

Appendix C Cloud regimes

We categorize output from the five GSAM simulations and satellite data from CERES into four different cloud regimes using cloud fraction and cloud top height from the M2005 MOD simulation. We do not use satellite observations to develop the cloud mask because both CERES and Himawari report cloud fractions near 1.0 in both open cell cumulus and stratiform cloud regions, so it cannot be used to distinguish these two regimes.

In order to avoid removing the majority of the data from our comparisons, we use GSAM output to develop the cloud mask. Because all five GSAM simulations are nudged by the same reanalysis, they typically simulate the same cloud morphologies in the same locations. Hence we can use the output from one simulation to develop a cloud mask that can be applied to all five simulations.

M2005 MOD and Thompson have the highest contrast in cloud fraction between stratus and cumulus regions (Figure 2), which make them good candidates for developing the cloud mask. However, Thompson stores most of its frozen hydrometeor mass in the snow class, and precipitation is not taken into account in the calculation of cloud top height in GSAM so Thompson often has a low bias in the cloud top height. Thus, we base the cloud mask on M2005 MOD.

We break the model output into 1° x 1° boxes (to compare with the CERES data, which is gridded at this resolution) and compute the average cloud fraction and cloud top height for each box. We use the decision tree in Figure C1 to classify each box into one of four regimes. We have hourly output from GSAM and we produce cloud masks for each hour. Examples of the resulting cloud mask for times during RF11 and RF12 are shown in Figure C2, overlaid on the albedo maps shown in Figure 2 as a visual check on the cloud mask. Note that we expect the best correspondence for M2005 MOD, which was used to derive the mask.

Acknowledgments

The authors gratefully acknowledge funding from U.S. National Science Foundation (NSF) grants AGS-1660604, AGS-1660609, and OISE-1743753. All simulations were performed using Cheyenne supercomputer (doi:10.5065/D6RX99HX) provided by NCAR's Computational and Information Systems Laboratory, sponsored by the NSF. We thank

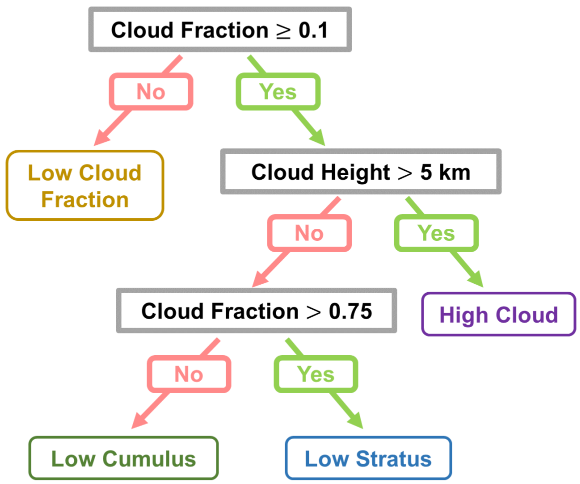

Figure C1. Decision tree for classifying 1° x 1° boxes into four different cloud regimes based on model output.

all the SOCRATES scientists and NCAR EOL for collecting the data and helping us interpret it, and Greg McFarquhar for his leadership in organizing the microphysical measurements. We additionally thank Paul DeMott, Emma Jrvinen, Christina McCluskey and Sonia Lasher-Trapp for helpful discussions about primary and secondary ice production during SOCRATES, and how these processes are represented in models. We thank Xiaoli Zhou for cleaning the HIAPER radar data and William Smith and the satCORPS team for reprocessing the Himawari analyses with tuning to monthly CERES data. We also thank Litai Kang and Roger Marchand for facilitating communication with the satCORPS team and for their helpful feedback on this work. We thank Hugh Morrison for sharing his discussion of M2005 and P3 schemes.

Data availability: CERES products used here can be downloaded at `https://ceres.larc.nasa.gov/data/`. Himawari products and all SOCRATES measurements used here can be downloaded at `https://data.eol.ucar.edu/master_lists/generated/socrates/`. GSAM model output cannot be made available due to the experimental nature of the simulations and the large storage space required. Our modified QUICKBEAM code can be accessed at `https://github.com/cloudatlas-on-github/QUICKBEAM-python`.

References

Atlas, R. L., Bretherton, C. S., Blossey, P. N., Gettelman, A., Bardeen, C.,

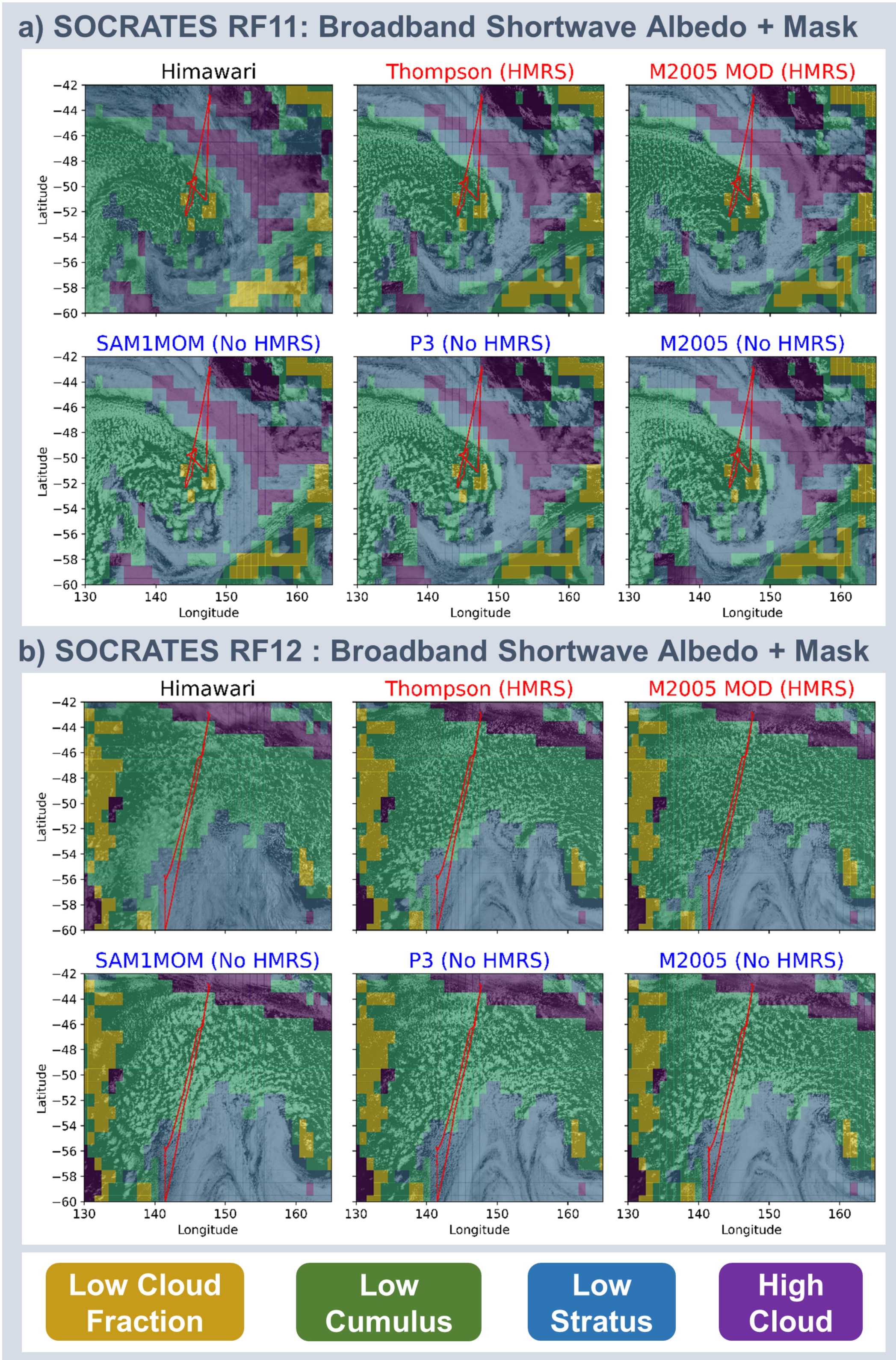

Figure C2. Cloud mask overlaid on the snapshots of visible albedo shown in Figure 2.

Lin, P., & Ming, Y. (2020). How well do large-eddy simulations and global climate models represent observed boundary layer structures and low clouds over the summertime southern ocean? [Journal Article]. *Journal of Advances in Modeling Earth Systems*, *12*(11), e2020MS002205. doi: https://doi.org/10.1029/2020MS002205

Atlas, R. L., Mohrmann, J., Finlon, J., Lu, J., Hsiao, I., Wood, R., & Diao, M. (2021). The University of Washington Ice-Liquid Discriminator (UWILD) improves single particle phase classifications of hydrometeors within Southern Ocean clouds using machine learning [preprint]. *Atmospheric Measurement Techniques Discussions*, *in review*, e2020EA001241. doi: https://doi.org/10.5194/amt-2021-123

Bergeron, T. (1928). ber die dreidimensional verknpfende wetteranalyse [Journal Article]. *Geophys. Norv.*, *5*(6), 1-111.

Bigg, E. K. (1953). The formation of atmospheric ice crystals by the freezing of droplets [Journal Article]. *Quarterly Journal of the Royal Meteorological Society*, *79*(342), 510-519. doi: https://doi.org/10.1002/qj.49707934207

Bony, S., Schulz, H., Vial, J., & Stevens, B. (2020). Sugar, gravel, fish, and flowers: Dependence of mesoscale patterns of trade-wind clouds on environmental conditions [Journal Article]. *Geophysical Research Letters*, *47*(7), e2019GL085988. doi: https://doi.org/10.1029/2019GL085988

Brewer, A. W., & Palmer, H. P. (1949). Condensation processes at low temperatures, and the production of new sublimation nuclei by the splintering of ice [Journal Article]. *Nature*, *164*(4164), 312-313. doi: 10.1038/164312a0

Collins, W. D., Rasch, P. J., Boville, B. A., Hack, J. J., McCaa, J. R., Williamson, D. L., … Zhang, M. (2006). The formulation and atmospheric simulation of the community atmosphere model version 3 (cam3) [Journal Article]. *Journal of Climate*, *19*(11), 2144-2161. Retrieved from `https://journals.ametsoc.org/view/journals/clim/19/11/jcli3760.1.xml` doi: 10.1175/jcli3760.1

Cooper, W. A. (1986). Ice initiation in natural clouds [Journal Article]. *Meteorological Monographs*, *21*(43), 29-32. doi: 10.1175/0065-9401-21.43.29

DeMott, P. J., Hill, T. C. J., McCluskey, C. S., Prather, K. A., Collins, D. B., Sullivan, R. C., … Franc, G. D. (2016). Sea spray aerosol as a unique source of ice nucleating particles [Journal Article]. *Proceedings of the National Academy of Sciences*, *113*(21), 5797-5803. Retrieved from `https://www.pnas.org/content/pnas/113/21/5797.full.pdf` doi: 10.1073/pnas.1514034112

Doelling, D. R., Loeb, N. G., Keyes, D. F., Nordeen, M. L., Morstad, D., Nguyen, C., ... Sun, M. (2013). Geostationary enhanced temporal interpolation for ceres flux products [Journal Article]. *Journal of Atmospheric and Oceanic Technology*, *30*(6), 1072-1090. doi: 10.1175/jtech-d-12-00136.1

EOL. (2018). *Ncar hcr radar time series data. version 1.0.* UCAR/NCAR - Earth Observing Laboratory. Retrieved from `https://data.eol.ucar.edu/dataset/552.022` doi: 10.5065/D6D7998S

EOL. (2019). *Low rate (lrt - 1 sps) navigation, state parameter, and microphysics flight-level data. version 1.3.* UCAR/NCAR EOL. Retrieved from `https://data.eol.ucar.edu/dataset/552.002` doi: 10.5065/D6M32TM9

Field, P. R., Lawson, R. P., Brown, P. R. A., Lloyd, G., Westbrook, C., Moisseev, D., ... Sullivan, S. (2016). Chapter 7. secondary ice production - current state of the science and recommendations for the future [Journal Article]. *Meteorological Monographs*, *58*, D-16-0014.1. doi: 10.1175/AMSMONOGRAPHS-D-16-0014.1

Gettelman, A., Bardeen, C. G., McCluskey, C. S., Jrvinen, E., Stith, J., Bretherton, C., ... Wu, W. (2020). Simulating observations of southern ocean clouds and implications for climate [Journal Article]. *Journal of Geophysical Research: Atmospheres*, *125*(21), e2020JD032619. doi: https://doi.org/10.1029/2020JD032619

Hallett, J., & Mossop, S. C. (1974). Production of secondary ice particles during riming process [Journal Article]. *Nature*, *249*(5452), 26-28. doi: 10.1038/249026a0

Haynes, J. M., Marchand, R. T., Luo, Z., Bodas-Salcedo, A., & Stephens, G. L. (2007). A multipurpose radar simulation package: Quickbeam [Journal Article]. *Bulletin of the American Meteorological Society*, *88*(11), 1723-1728. doi: 10.1175/bams-88-11-1723

Heymsfield, A., & Willis, P. (2014). Cloud conditions favoring secondary ice particle production in tropical maritime convection [Journal Article]. *Journal of the Atmospheric Sciences*, *71*(12), 4500-4526. doi: 10.1175/jas-d-14-0093.1

Hobbs, P. V., & Rangno, A. L. (1985). Ice particle concentrations in clouds [Journal Article]. *Journal of Atmospheric Sciences*, *42*(23), 2523-2549. doi: 10.1175/1520-0469(1985)042⟨2523:ipcic⟩2.0.co;2

Huang, Y., Chubb, T., Baumgardner, D., Dehoog, M., Siems, S. T., & Manton, M. J. (2017). Evidence for secondary ice production in southern ocean open cellular convection [Journal Article]. *Quarterly Journal of the Royal Meteorological Society*, *143*(704), 1685-1703. doi: 10.1002/qj.3041

Khairoutdinov, M. F., & Randall, D. A. (2003). Cloud resolving modeling of the arm summer 1997 iop: Model formulation, results, uncertainties, and sensitivities [Journal Article]. *Journal of the Atmospheric Sciences*, *60*(4), 607-625. doi: 10.1175/1520-0469(2003)060⟨0607:crmota⟩2.0.co;2

Koenig, L. R. (1963). The glaciating behavior of small cumulonimbus clouds [Journal Article]. *Journal of Atmospheric Sciences*, *20*(1), 29-47. doi: 10.1175/1520-0469(1963)020⟨0029:tgbosc⟩2.0.co;2

Ladino, L. A., Korolev, A., Heckman, I., Wolde, M., Fridlind, A. M., & Ackerman, A. S. (2017). On the role of ice-nucleating aerosol in the formation of ice particles in tropical mesoscale convective systems [Journal Article]. *Geophysical Research Letters*, *44*(3), 1574-1582. doi: https://doi.org/10.1002/2016GL072455

Luke, E. P., Yang, F., Kollias, P., Vogelmann, A. M., & Maahn, M. (2021). New insights into ice multiplication using remote-sensing observations of slightly supercooled mixed-phase clouds in the arctic [Journal Article]. *Proceedings of the National Academy of Sciences*, *118*(13), e2021387118. doi: 10.1073/pnas.2021387118

McCluskey, C. S., DeMott, P. J., Ma, P.-L., & Burrows, S. M. (2019). Numerical representations of marine ice-nucleating particles in remote marine environments evaluated against observations [Journal Article]. *Geophysical Research Letters*, *46*(13), 7838-7847. Retrieved from `https://agupubs.onlinelibrary.wiley.com/doi/abs/10.1029/2018GL081861` doi: https://doi.org/10.1029/2018GL081861

McCluskey, C. S., Hill, T. C. J., Humphries, R. S., Rauker, A. M., Moreau, S., Strutton, P. G., ... DeMott, P. J. (2018). Observations of ice nucleating particles over southern ocean waters [Journal Article]. *Geophysical Research Letters*, *45*(21), 11,989-11,997. doi: https://doi.org/10.1029/2018GL079981

McFarquhar, G., Bretherton, C., Marchand, R., Protat, A., Demott, P., Alexander, S., . . . McDonald, A. (2020). Observations of clouds, aerosols, precipitation, and surface radiation over the southern ocean: An overview of capricorn, marcus, micre and socrates [Journal Article]. *Bulletin of the American Meteorological Studies*.

Meyers, M. P., DeMott, P. J., & Cotton, W. R. (1992). New primary ice-nucleation parameterizations in an explicit cloud model [Journal Article]. *Journal of Applied Meteorology and Climatology*, *31*(7), 708-721. doi: 10.1175/1520-0450(1992)031⟨0708:npinpi⟩2.0.co;2

Mitchell, J. F. B., Senior, C. A., & Ingram, W. J. (1989). C02 and climate: a missing feedback? [Journal Article]. *Nature*, *341*(6238), 132-134. doi: 10.1038/341132a0

Morrison, H., Curry, J. A., & Khvorostyanov, V. I. (2005). A new double-moment microphysics parameterization for application in cloud and climate models. part i: Description [Journal Article]. *Journal of the Atmospheric Sciences*, *62*(6), 1665-1677. doi: 10.1175/jas3446.1

Morrison, H., & Milbrandt, J. A. (2015). Parameterization of cloud microphysics based on the prediction of bulk ice particle properties. part i: Scheme description and idealized tests [Journal Article]. *Journal of the Atmospheric Sciences*, *72*(1), 287-311. doi: 10.1175/jas-d-14-0065.1

NASA/LARC/SD/ASDC. (2017). *Ceres and geo-enhanced toa, within-atmosphere and surface fluxes, clouds and aerosols 1-hourly terra edition4a.* NASA Langley Atmospheric Science Data Center DAAC. Retrieved from `https://doi.org/10.5067/TERRA+AQUA/CERES/SYN1DEG-1HOUR_L3.004A` doi: 10.5067/TERRA+AQUA/CERES/SYN1DEG-1HOUR_L3.004A

Pruppacher, H. R., Klett, J. D., & SpringerLink. (2010). *Microphysics of clouds and precipitation* (1. ed.) [Book]. Dordrecht: Springer Netherlands.

Rangno, A. L., & Hobbs, P. V. (2001). Ice particles in stratiform clouds in the arctic and possible mechanisms for the production of high ice concentrations [Journal Article]. *Journal of Geophysical Research-Atmospheres*, *106*(D14), 15065-15075. doi: 10.1029/2000jd900286

Rogers, R. R., & Yau, M. K. (1996). *A short course in cloud physics* (Third edition. ed.) [Book]. Burlington, Massachusetts: Butterworth-Heinemann.

Scott, E. L. (2019). *The influence of primary nucleation and rime splintering on ice number concentrations in southern ocean cumuli* (Thesis).

Smith, W., & Minnis, P. (2020). *Nasa satcorps himawari cloud retrieval data. version 2.2.* UCAR/NCAR - Earth Observing Laboratory. Retrieved from `https://data.eol.ucar.edu/dataset/552.027` doi: 10.5065/D6CC0ZFJ

Sotiropoulou, G., Sullivan, S., Savre, J., Lloyd, G., Lachlan-Cope, T., Ekman, A. M. L., & Nenes, A. (2020). The impact of secondary ice production on arctic stratocumulus [Journal Article]. *Atmos. Chem. Phys.*, *20*(3), 1301-1316. doi: 10.5194/acp-20-1301-2020

Sotiropoulou, G., Vignon, E., Young, G., Morrison, H., O'Shea, S. J., Lachlan-Cope, T., ... Nenes, A. (2021). Secondary ice production in summer clouds over the antarctic coast: an underappreciated process in atmospheric models [Journal Article]. *Atmos. Chem. Phys.*, *21*(2), 755-771. doi: 10.5194/acp-21-755-2021

Stevens, B., Bony, S., Brogniez, H., Hentgen, L., Hohenegger, C., Kiemle, C., ... Zuidema, P. (2020). Sugar, gravel, fish and flowers: Mesoscale cloud patterns in the trade winds [Journal Article]. *Quarterly Journal of the Royal Meteorological Society*, *146*(726), 141-152. doi: https://doi.org/10.1002/qj.3662

Stevens, B., Satoh, M., Auger, L., Biercamp, J., Bretherton, C. S., Chen, X., ... Zhou, L. (2019). Dyamond: the dynamics of the atmospheric general circulation modeled on non-hydrostatic domains [Journal Article]. *Progress in Earth and Planetary Science*, *6*(1), 61. doi: 10.1186/s40645-019-0304-z

Sun, Z., & Shine, K. P. (1994). Studies of the radiative properties of ice and mixed-phase clouds [Journal Article]. *Quart. J. Roy. Meteor. Soc.*, *120*, 111-137. doi: 10.1002/qj.49712051508

Taylor, J. W., Choularton, T. W., Blyth, A. M., Liu, Z., Bower, K. N., Crosier, J., ... Brown, P. R. A. (2016). Observations of cloud microphysics and ice formation during cope [Journal Article]. *Atmos. Chem. Phys.*, *16*(2), 799-826. doi: 10.5194/acp-16-799-2016

Thompson, G., Field, P. R., Rasmussen, R. M., & Hall, W. D. (2008). Explicit forecasts of winter precipitation using an improved bulk microphysics scheme. part ii: Implementation of a new snow parameterization [Journal Article]. *Monthly Weather Review*, *136*(12), 5095-5115. doi: 10.1175/2008mwr2387.1

Trenberth, K. E., & Fasullo, J. T. (2010). Simulation of present-day and twentyfirst-century energy budgets of the southern oceans [Journal Article]. *Journal of Climate*, *23*(2), 440-454. doi: 10.1175/2009jcli3152.1

Vergara-Temprado, J., Miltenberger, A. K., Furtado, K., Grosvenor, D. P., Shipway, B. J., Hill, A. A., ... Carslaw, K. S. (2018). Strong control of southern ocean cloud reflectivity by ice-nucleating particles [Journal Article]. *Proceedings of the National Academy of Sciences*, *115*(11), 2687-2692. doi: 10.1073/pnas.1721627115

Vonder Haar, T. H., & Suomi, V. E. (1971). Measurements of the earth's radiation budget from satellites during a five-year period. part i: Extended time and space means [Journal Article]. *Journal of Atmospheric Sciences*, *28*(3), 305-314. doi: 10.1175/1520-0469(1971)028⟨0305:moterb⟩2.0.co;2

Young, G., Lachlan-Cope, T., O'Shea, S. J., Dearden, C., Listowski, C., Bower, K. N., ... Gallagher, M. W. (2019). Radiative effects of secondary ice enhancement in coastal antarctic clouds [Journal Article]. *Geophysical Research Letters*, *46*(4), 2312-2321. doi: 10.1029/2018gl080551

Zhou, X., Atlas, R., McCoy, I. L., Bretherton, C. S., Bardeen, C., Gettelman, A., ... Ming, Y. (2021). Evaluation of cloud and precipitation simulations in cam6 and am4 using observations over the southern ocean [Journal Article]. *Earth and Space Science*, *8*(2), e2020EA001241. doi: https://doi.org/10.1029/2020EA001241

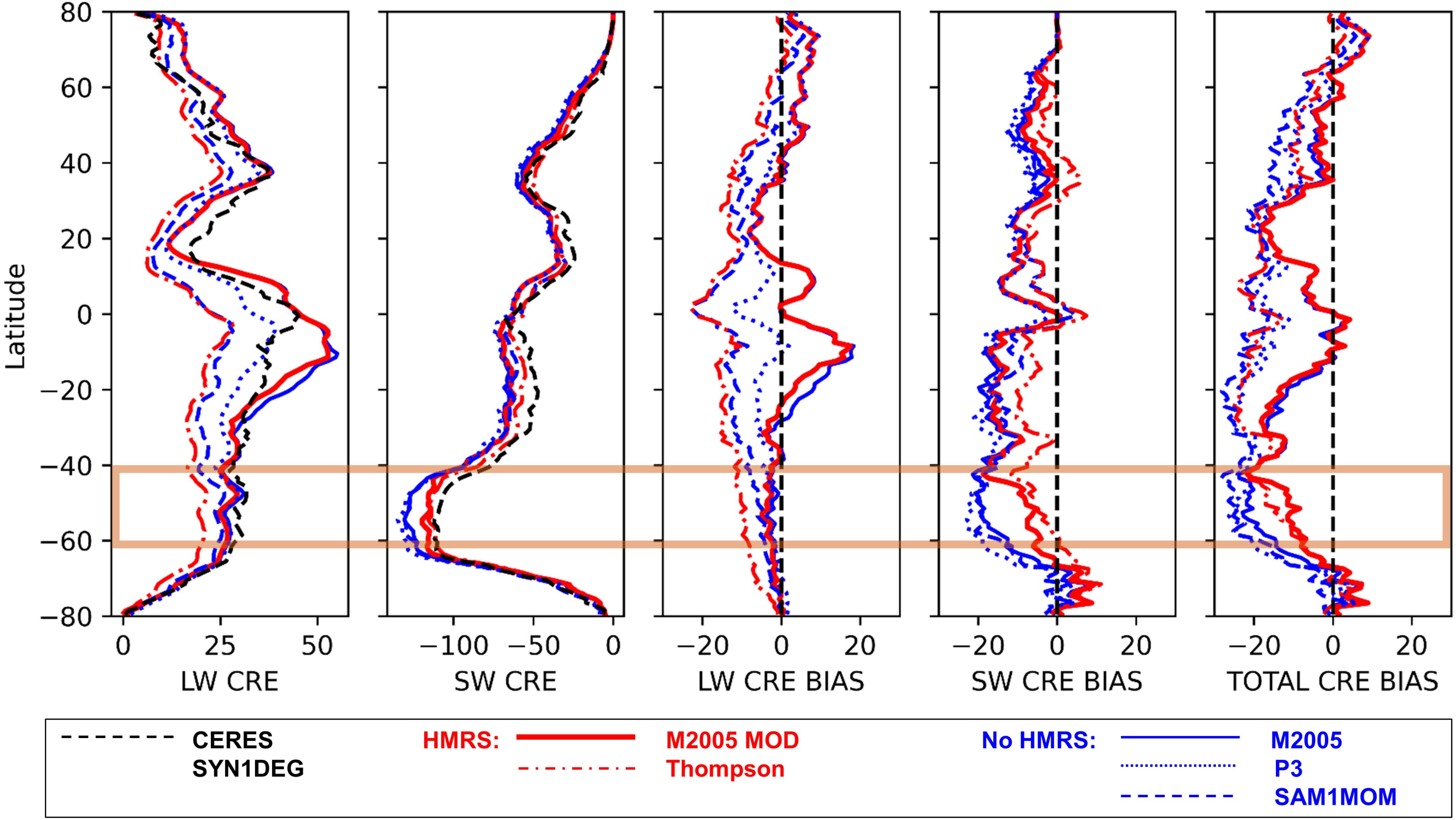

80
60
40
20
0
−20
−40
−60
−80
Latitude
0
25
50
LW CRE
−100
−50
0
SW CRE
−20
0
20
LW CRE BIAS
−20
0
20
SW CRE BIAS
−20
0
20
TOTAL CRE BIAS
CERES
SYN1DEG
HMRS:
M2005 MOD
Thompson
No HMRS:
M2005
P3
SAM1MOM

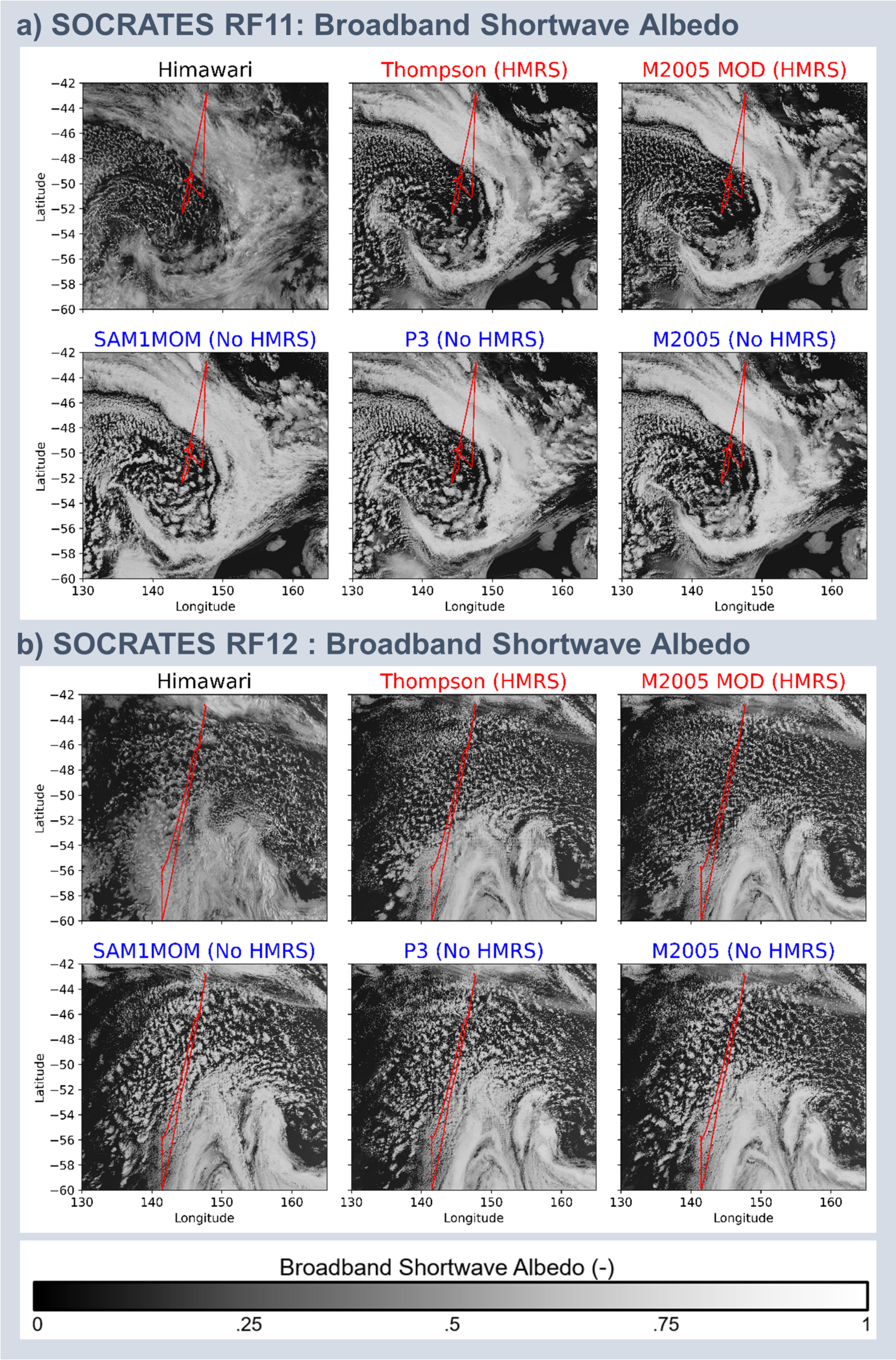
a) SOCRATES RF11: Broadband Shortwave Albedo
Himawari
Thompson (HMRS)
M2005 MOD (HMRS)
SAM1MOM (No HMRS)
P3 (No HMRS)
M2005 (No HMRS)
Latitude
Longitude
−42
−44
−46
−48
−50
−52
−54
−56
−58
−60
130
140
150
160
b) SOCRATES RF12 : Broadband Shortwave Albedo
Himawari
Thompson (HMRS)
M2005 MOD (HMRS)
SAM1MOM (No HMRS)
P3 (No HMRS)
M2005 (No HMRS)
Latitude
Longitude
Broadband Shortwave Albedo (-)
0
.25
.5
.75
1

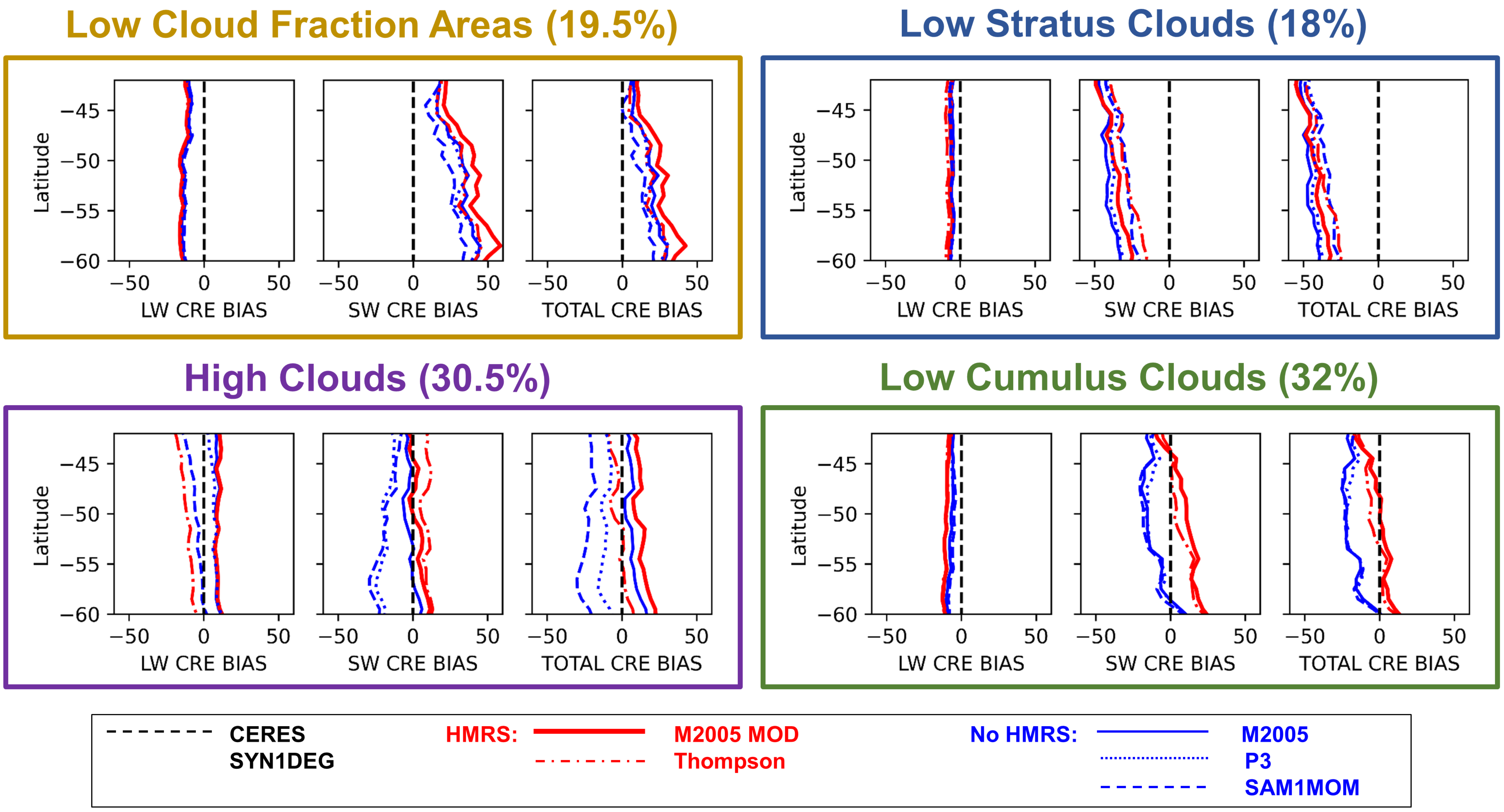

Low Cloud Fraction Areas (19.5%)
Low Stratus Clouds (18%)
High Clouds (30.5%)
Low Cumulus Clouds (32%)
Latitude
−45
−50
−55
−60
−50
0
50
LW CRE BIAS
SW CRE BIAS
TOTAL CRE BIAS
CERES SYN1DEG
HMRS:
M2005 MOD
Thompson
No HMRS:
M2005
P3
SAM1MOM

SOCRATES RF12: Particle Size Distributions

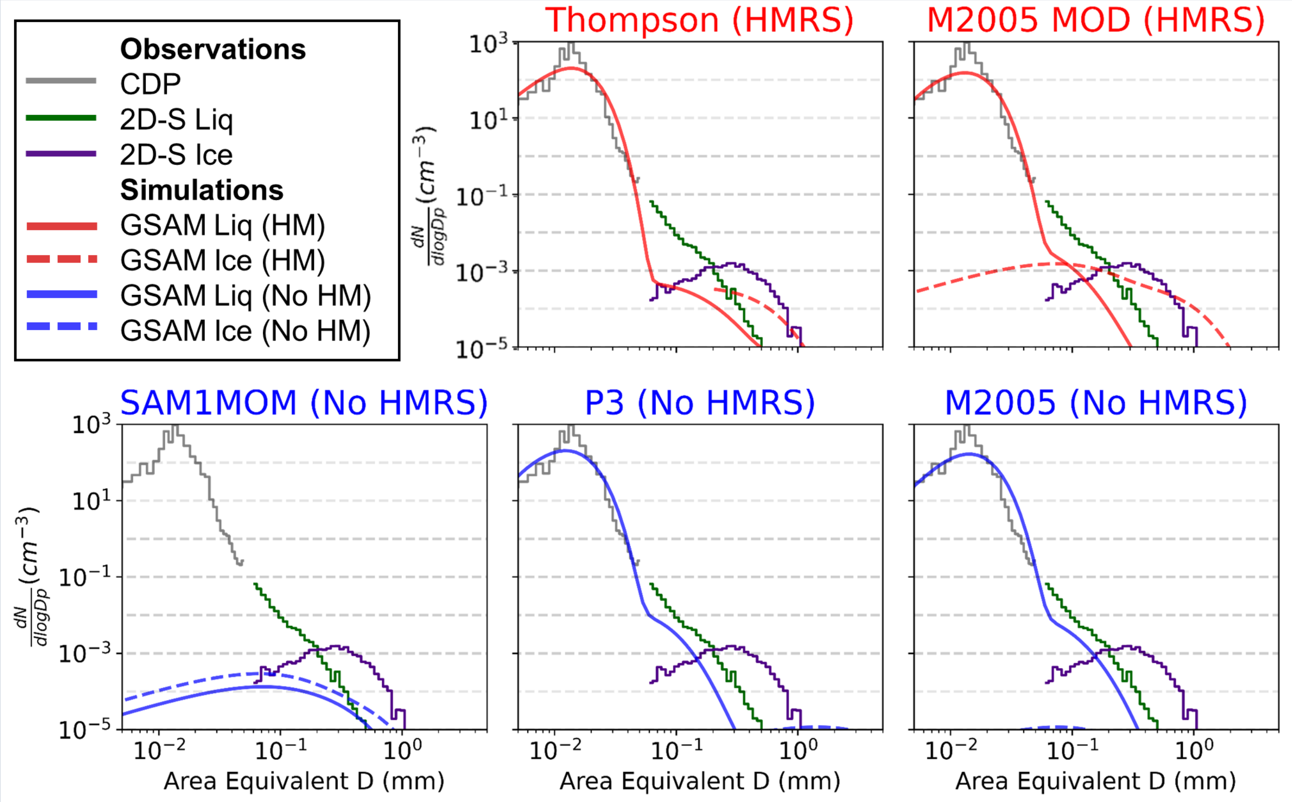

SOCRATES RF11 : Radar Reflectivity

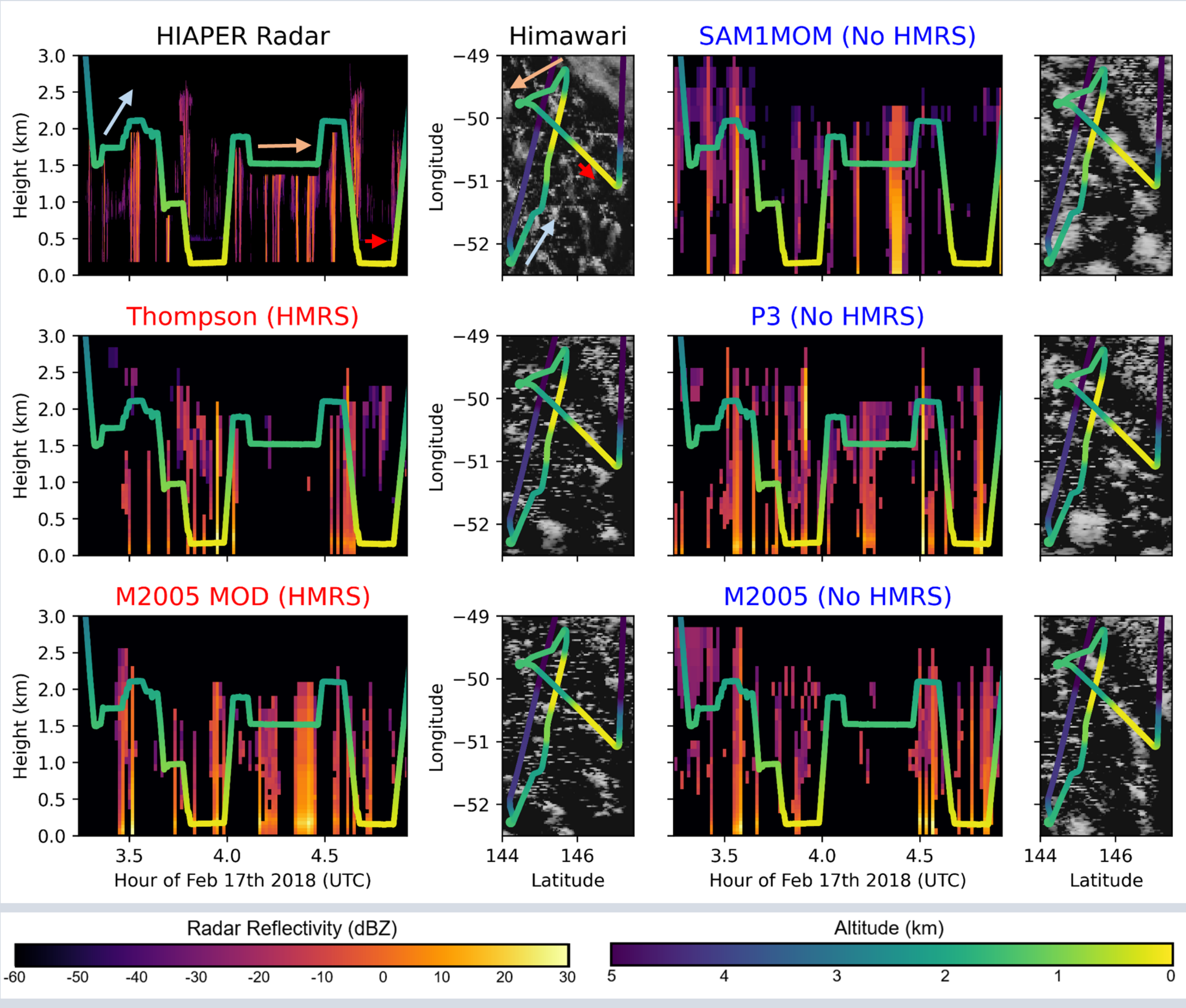

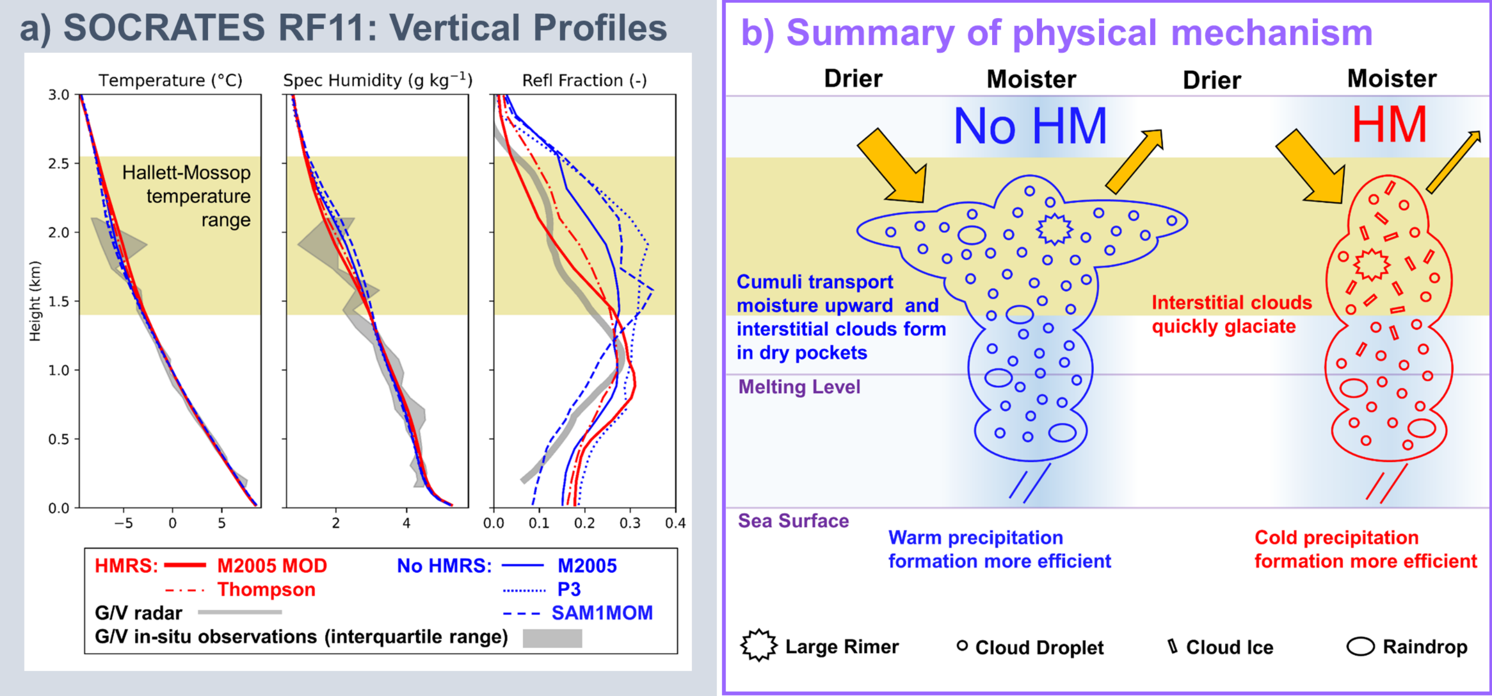

a) SOCRATES RF11: Vertical Profiles
Temperature (°C)
Spec Humidity (g kg⁻¹)
Refl Fraction (-)
Height (km)
Hallett-Mossop temperature range
HMRS:
M2005 MOD
Thompson
No HMRS:
M2005
P3
SAM1MOM
G/V radar
G/V in-situ observations (interquartile range)
b) Summary of physical mechanism
Drier
Moister
Drier
Moister
No HM
HM
Cumuli transport moisture upward and interstitial clouds form in dry pockets
Interstitial clouds quickly glaciate
Melting Level
Sea Surface
Warm precipitation formation more efficient
Cold precipitation formation more efficient
Large Rimer
Cloud Droplet
Cloud Ice
Raindrop

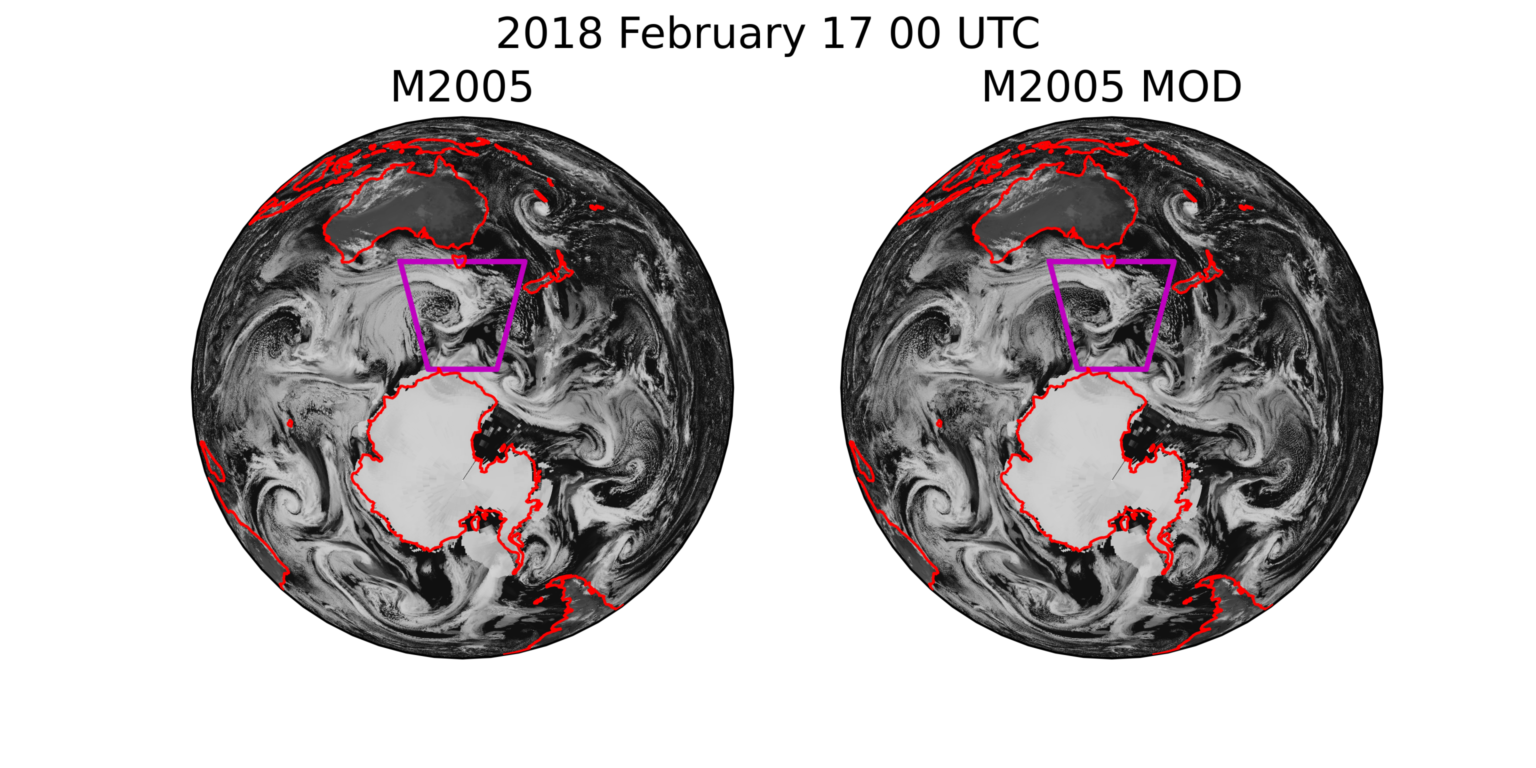
2018 February 17 00 UTC
M2005
M2005 MOD

Ice crystals (SOCRATES RF11 and RF12) and marine INP concentrations

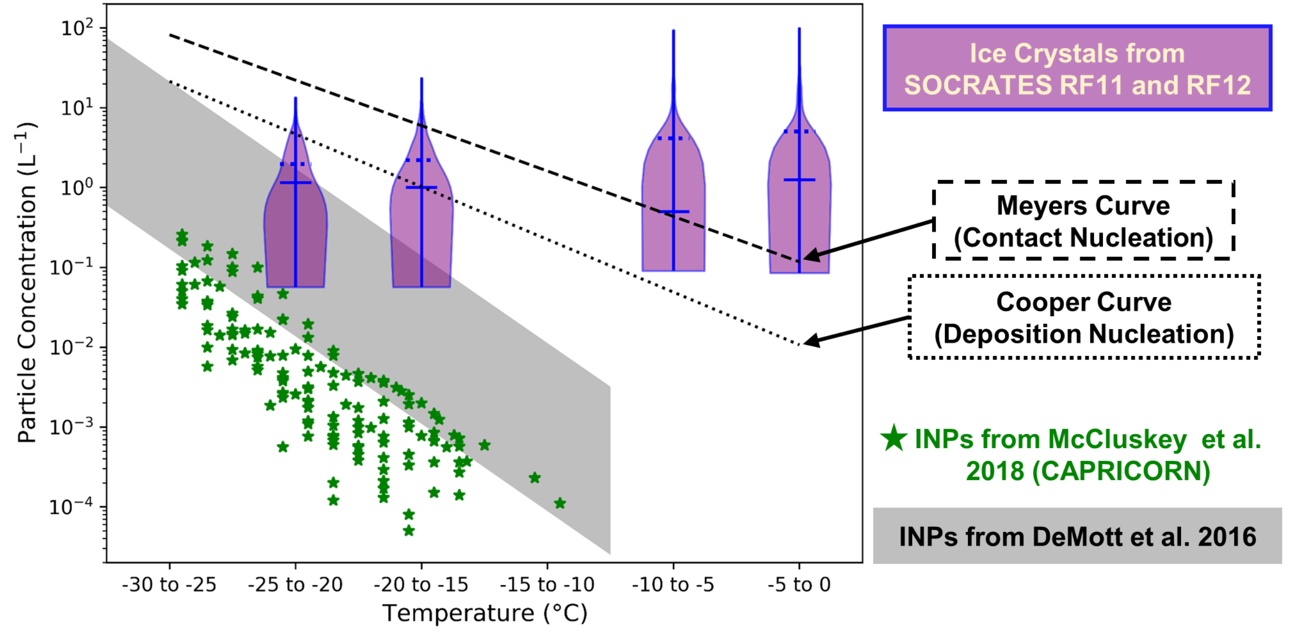

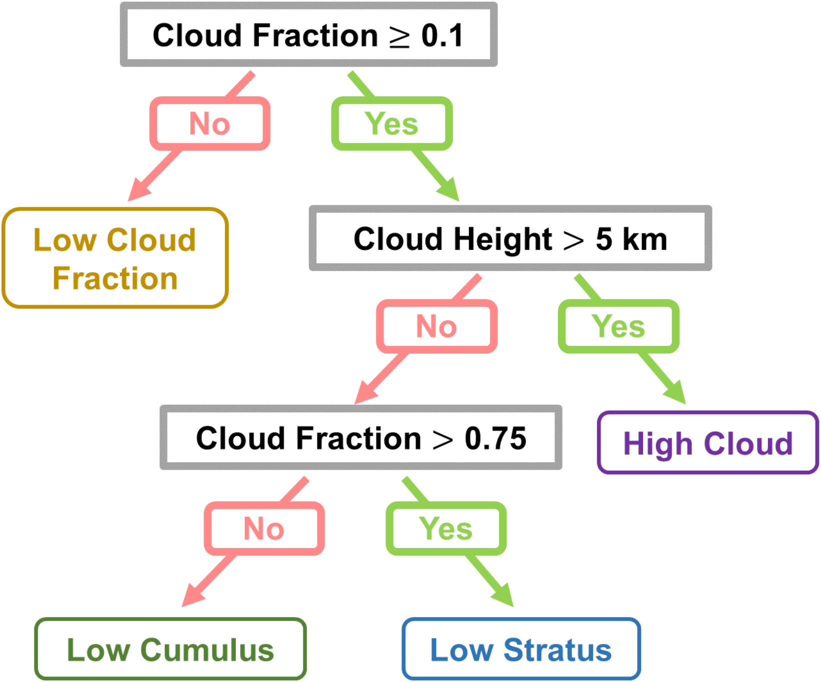
Cloud Fraction ≥ 0.1
No
Yes
Low Cloud Fraction
Cloud Height > 5 km
No
Yes
Cloud Fraction > 0.75
High Cloud
No
Yes
Low Cumulus
Low Stratus

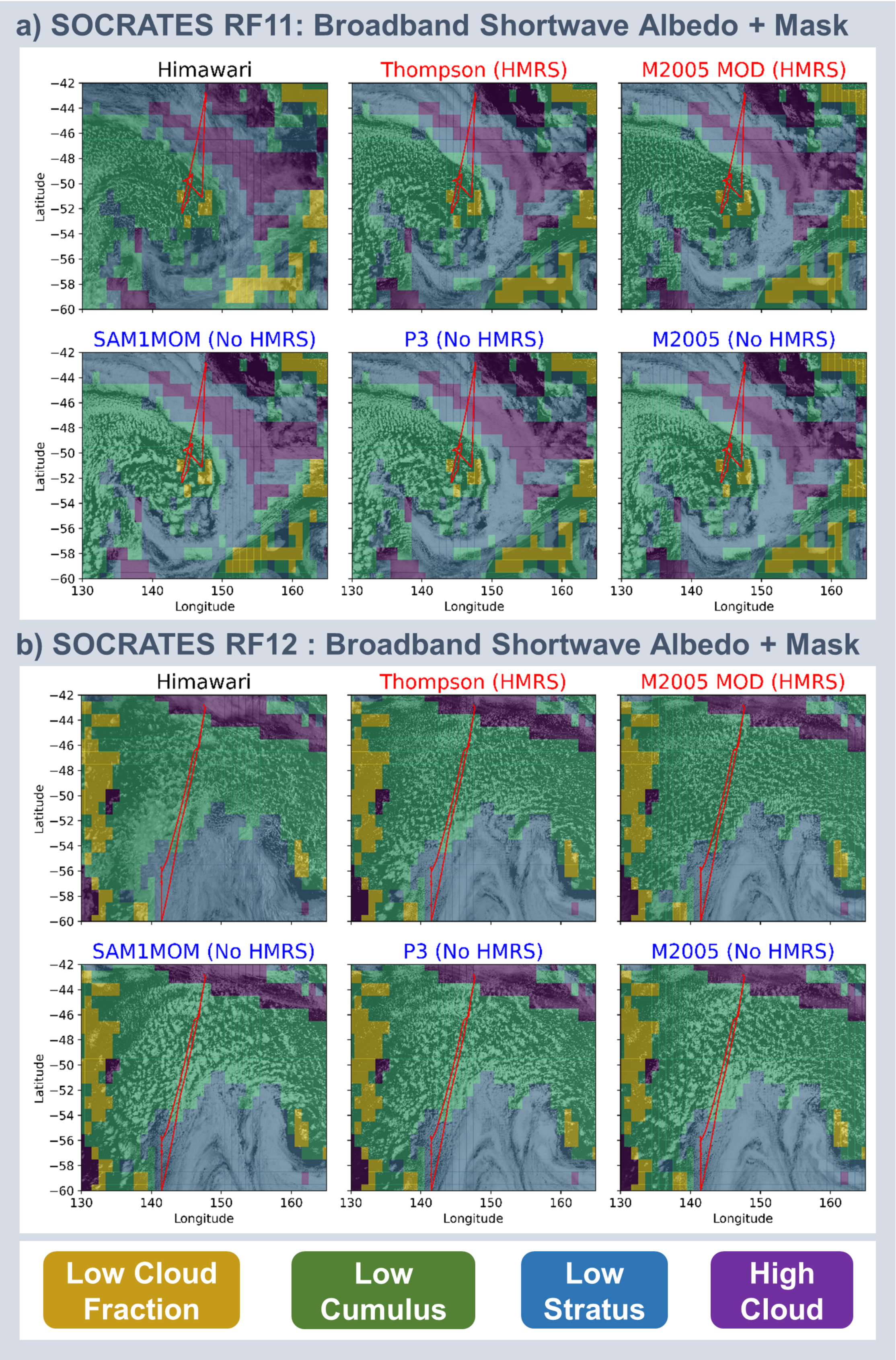

a) SOCRATES RF11: Broadband Shortwave Albedo + Mask
Himawari
Thompson (HMRS)
M2005 MOD (HMRS)
SAM1MOM (No HMRS)
P3 (No HMRS)
M2005 (No HMRS)
Latitude
Longitude
b) SOCRATES RF12 : Broadband Shortwave Albedo + Mask
Low Cloud Fraction
Low Cumulus
Low Stratus
High Cloud